Mass Accretion, Spectral, and Photometric Properties of T Tauri Stars in Taurus Based on TESS and LAMOST

Chia-Lung Lin[1] , Wing-Huen Ip[1,2] , Yao Hsiao[1] , Tzu-Hueng Chang[1], Yi-han Song[3] , and A-Li Luo[3]

[1] Graduate Institute of Astronomy, National Central University, Taoyuan 32001, Taiwan
[2] Graduate Institute of Space Science, National Central University, Taoyuan 32001, Taiwan
[3] Key Laboratory of Optical Astronomy, National Astronomical Observatories, Chinese Academy of Sciences, Beijing 100012, People's Republic of China

Abstract

We present the analysis of 16 classical T Tauri stars (CTTSs) using LAMOST and TESS data, investigating spectral properties, photometric variations, and mass accretion rates. All 16 stars exhibit emissions in Hα lines, from which the average mass accretion rate of 1.76×10^{-9} $M_\odot$ yr^{-1} is derived. Two of the stars, DL Tau and Haro 6-13, show mass accretion bursts simultaneously in TESS, ASAS-SN, and/or the ZTF survey. Based on these observations, we find that the mass accretion rates of DL Tau and Haro 6-13 reach their maxima of 2.5×10^{-8} $M_\odot$ yr^{-1} and 2×10^{-10} $M_\odot$ yr^{-1}, respectively, during the TESS observation. We detect 13 flares among these stars. The flare frequency distribution shows that the CTTSs' flare activity is not only dominated by strong flares with high energy but also much more active than those of solar-type and young low-mass stars. By comparing the variability classes reported in the literature, we find that the transition timescale between different classes of variability in CTTSs, such as from stochastic (S) to bursting (B) or from quasi-periodic symmetric to quasi-periodic dipping, may range from 1.6 to 4 yr. We observe no significant correlation between inclination and mass accretion rates derived from the emission indicators. This suggests that inner disk properties may be more important than those of outer disks. Finally, we find a relatively significant positive correlation between the asymmetric metric M and the cold disk inclination compared to the literature. A weak negative correlation between the periodicity metric Q value and inclination has also been found.

Unified Astronomy Thesaurus concepts: Star formation (1569); Young stellar objects (1834); Low mass stars (2050); Classical T Tauri stars (252); Stellar flares (1603)

1. Introduction

Classical T Tauri stars (CTTSs) are young, low-mass pre-main-sequence objects with typical spectral types between F and M that are accreting material from the circumstellar disk. These stars exhibit strong emission lines in their spectra and show an excess of emission ranging from radio to ultraviolet relative to the stellar photosphere. The infrared excess emission from CTTSs indicates the presence of a circumstellar disk (Mendoza 1968; Lynden-Bell & Pringle 1974; Adams et al. 1987; Bertout et al. 1988) and can be used to infer the amount of dust and the evolutionary status of the system. The amount of circumstellar material drops as the protostellar system evolves, leading to the decrease of the excess emission in the infrared.

The CTTSs have luminosity variations on different timescales, from hours to even decades (Rucinski et al. 2008; Cody et al. 2013), depending on various physical phenomena affecting the stellar and circumstellar environment. For example, the obscuration of the central star's photosphere by circumstellar dust may lead to an aperiodic dip of light (e.g., McGinnis et al. 2015). The presence of stable starspots on the stellar surface may result in a periodic modulation in the light curve of the star (e.g., Kóspál et al. 2018). The unsteady accretion processes and magnetic activity (i.e., flares) may cause the random and short-timescale brightening variability. The stochastic light curve of CTTSs may be attributed to the superposition of the various types of variability resulting from different mechanisms mentioned earlier. All these mechanisms can vary with time.

One of the major sources of variability in CTTSs during this evolutionary phase is the accretion-driven burst (e.g., Fischer et al. 2022). There are various types of accretion-driven bursts that last for different timescales. One type is the FU Ori–like outburst, which is characterized by a large increase in luminosity (typically by a factor of tens) over a timescale of decades to hundreds of years (e.g., Clarke et al. 2005). In addition, the outbursts with the type of V1647 Ori, EX Lup, and protostellar share a similar timescale of a few years, with a luminosity increase ranging from 1 to 5 mag. Lastly, the one we focus on in this study is the accretion burst with a luminosity variability up to a few magnitudes on a relatively short timescale from a few hours to days at optical wavelengths (e.g., Cody & Hillenbrand 2018). The numerical simulations carried out by Čemeljić & Siwak (2020) suggest that this variability could be caused by unstable accretion processes. In addition, such events, coupled with rotational modulation, tend to dominate changes in the accretion rate (Rigon et al. 2017; Sergison et al. 2020).

According to the magnetospheric accretion mechanism (e.g., Camenzind 1990), the most viable scenario currently used to describe the accretion behaviors of CTTSs, the central star is channeling the material in the circumstellar disk to the stellar surface through the magnetospheric accretion columns (Feigelson & Montmerle 1999; Muzerolle et al. 2003). The gas is heated to a temperature of 10^4–10^6 K when the channeled materials hit the stellar surface, creating a shock on the stellar photosphere, which emits intense X-rays (Argiroffi et al. 2007;

Günther et al. 2007; Costa et al. 2017). The X-rays are mostly reabsorbed by the accretion columns, from which the lower-energy photons, mainly in the blue band, are reemitted, resulting in a luminosity excess from visible to ultraviolet wavelengths. Thus, the U-band excess has often been used to determine the accretion luminosity, from which the mass accretion rate can be determined (Gullbring et al. 1998; Herczeg & Hillenbrand 2008). In addition, such an accretion mechanism also produces detectable emission features in CTTS spectra, such as Hα and Hβ (e.g., Basri & Bertout 1989). Sousa et al. (2016) show that when U-band excesses are not available, mass accretion rates can be obtained with good results from the Hα flux using the currently available calibrations from the literature. Therefore, these emission features can be used to probe the state (i.e., active or inactive) of the mass accretion process. Furthermore, multiband simultaneous observations can be useful for estimating the mass accretion rate of CTTSs even without direct U-band measurements. For example, Tofflemire et al. (2017) and Kóspál et al. (2018) used optical wavelength observations of accretion burst variability to estimate the mass accretion rate of DQ Tau. Kóspál et al. (2018) used the Kepler light curve to identify the burst phenomenons and extrapolated the associated U-band excess luminosities based on the simultaneous $BVRI$ observations of the star.

In this study, we present mass accretion rates and the properties that can be determined with our data for selected CTTSs in the Taurus Molecular Cloud (TMC), which is a nearby star-forming region located at a distance of about 147 pc from the Sun (Zucker et al. 2020) with an age of 1–3 Myr (Simon et al. 2017), using high photometric precision light curves and low-resolution spectra from the space-based Transiting Exoplanet Survey Satellite (TESS) and Large Sky Area Multi-Object Fiber Spectroscopic Telescope (LAMOST), respectively. Given the lengths of the available light-curve data, we will primarily focus on the short-timescale burst.

The outline of this paper is as follows. In Section 2, we introduce the TESS and LAMOST observations of TMC members, including their stellar parameters reported in the literature. In Section 3, we explain our methodology for estimating the mass accretion rates of our CTTS targets using various emission indicators from LAMOST low-resolution spectra and TESS light curves. We also detail our method for determining photometric variabilities in this section. In Section 4, we describe our results of the data analysis and implications. Finally, in Section 5, we summarize the results and conclude the study.

2. Sample and Data Sets

2.1. LAMOST Spectroscopic Survey on T Tauri Stars

LAMOST, located at the Xinglong Observatory of the National Astronomical Observatories of Chinese Academy of Sciences (NAOC), is a reflecting Schmidt telescope with an effective aperture of ∼4 m and a wide field of view of 20 deg^2 in the sky (Zhao et al. 2012).

With 4000 fibers that are mounted on the focal plane, it has been conducting spectroscopic surveys efficiently for stars, galaxies, and quasars mostly in the northern celestial hemi-sphere above the decl. of −10° since autumn 2012. Each fiber has a scale of 3″3 on the focal surface. The centers of the spectroscopic fibers are about 4″47 apart, and each fiber can

Table 1
16 CTTSs in TMC Observed by LAMOST and TESS

Name (1)	LAMOST Obser. Date (2)	TIC (3)
AA Tau	2019-01-29	268510757
BP Tau	2014-01-25	58287935
CI Tau	2016-02-07	61230756
DL Tau	2012-12-23	268444139
DN Tau	2012-12-23	268511247
DQ Tau	2020-01-26	436614017
FN Tau	2014-01-25	56625009
GG Tau	2016-02-05	245830955
GO Tau	2013-11-29	125914458
Haro 6-13	2012-12-23	268324608
HK Tau	2012-11-07	268324063
HL Tau	2013-02-09	353752575
IQ Tau	2012-12-23	268219495
UY Aur	2019-12-30	96205005
GI Tau	2019-01-29	268444803
HP Tau	2012-12-23	118521708

move at most 3′ from its center position. Sixteen spectrographs are used in the system, and each receives the dispersed light from 250 fibers. The resolution of LAMOST spectra is $R \approx$ 1800 around the Sloan Digital Sky Survey (SDSS) g band with a wavelength coverage of 3700–9100 Å.

The LAMOST 2D pipeline is utilized for data reduction. Initially, each exposure's data from each CCD chip are separately reduced, and then the results from each exposure are combined. Bias and dark are subtracted from each raw image. The flat-field spectrum of each fiber is traced, and a polynomial is fitted to the centroid of each fiber's row position. A Gaussian-like profile is assumed for each fiber's profile in the row direction. Using the same trace function, spectra are extracted from all data on the same night, with minor shifts made to align individual frames. The extracted spectra are divided by the one-dimensional flat-field spectrum. The Hg/Cd and Ne/Ar arc lamp spectra are also extracted using the same trace function, including strong sky emission lines to further improve the wavelength solution. The sky spectra are obtained from 20 sky fibers allocated in each spectrograph. After wavelength calibration, all sky spectra are combined into one supersky spectrum. The supersky spectrum is scaled to best fit the sky spectrum in each fiber, and then this scaled supersky is subtracted from each fiber, and the telluric absorption is removed. The science spectra are flux-calibrated by matching the selected flux standard stars and their templates, which are usually of spectral type A or F. Up to five flux standard stars are observed per spectrograph.

We retrieved spectroscopic data of CTTSs in the TMC from LAMOST's decade-long archive of observational data, and 16 targets are identified (see Table 1). The LAMOST low-resolution spectra of these CTTSs are shown in Figure 1. Table 2 contains the stellar parameters of our targets. The masses and radii of most CTTSs are provided in Herczeg & Hillenbrand (2014), with the exception of HL Tau. The radius ($R = 7 R_\odot$) and mass ($M = 1.7 M_\odot$) of HL Tau are given by Liu et al. (2017) and Pinte et al. (2016), respectively. The inclinations of the outer disk have been reported by the adaptive optics (i.e., Close et al. 1998), millimeter radio (i.e., Guilloteau et al. 1999), high-resolution near-infrared imaging (Kudo et al. 2008), and high-resolution submillimeter resolved
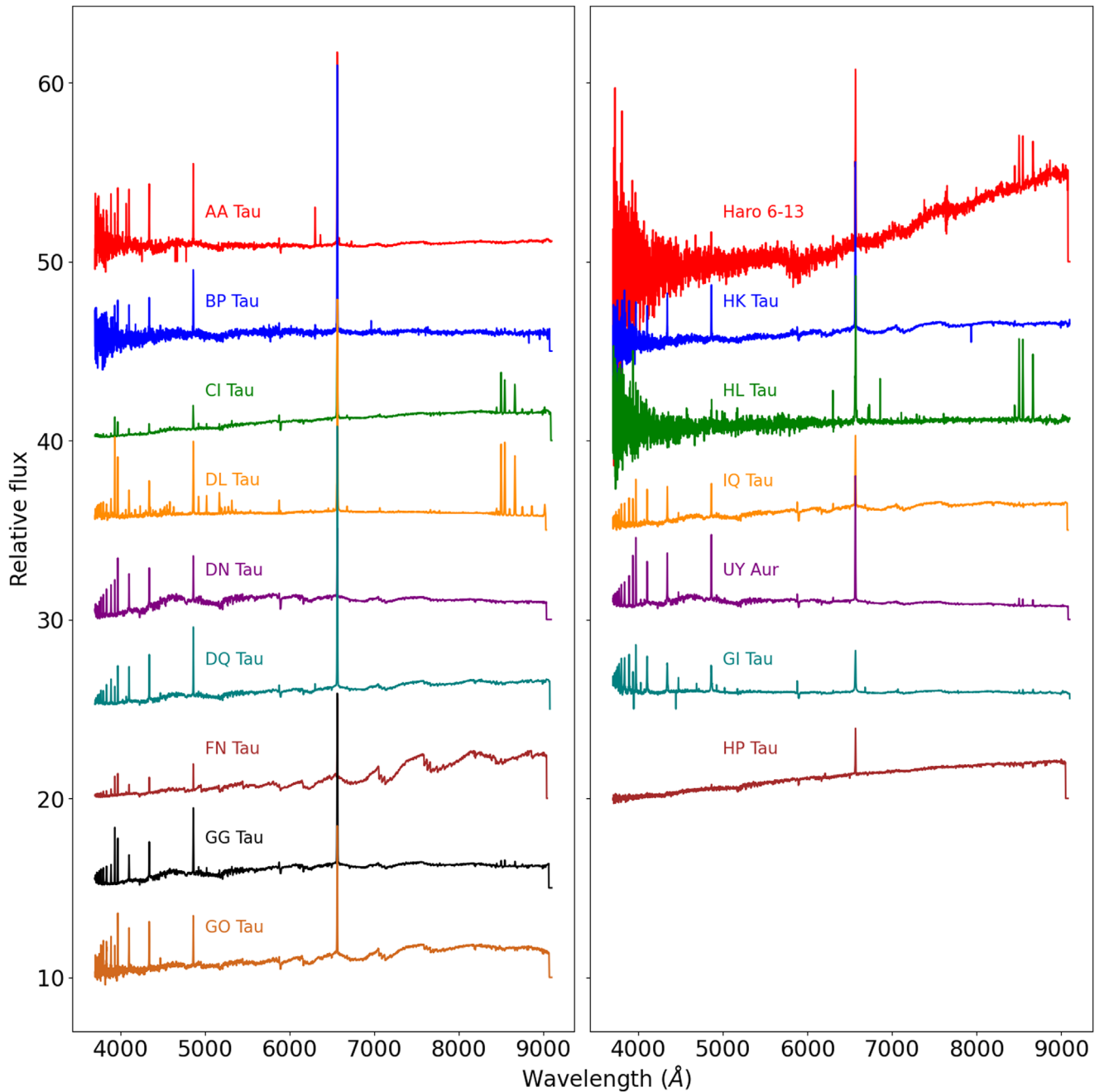
Figure 1. The LAMOST low-resolution spectra of 16 CTTSs in this study.

image observations of the TMC region (Partnership et al. 2015; Long et al. 2019; Manara et al. 2019; Villenave et al. 2020). The distance information for the objects studied in this work is from the parallax measurements reported in Gaia Collaboration (2020). HK Tau is a binary system consisting of two companions, HK Tau A and HK Tau B, with HK Tau A being much brighter than HK TauB ($G = 14.106$ vs. $G = 17.962$; Gaia Collaboration et al. 2021). The disk inclinations of the two companions are highly misaligned, with HK Tau A having an inclination of $i = 56°.9$ (Manara et al. 2019) and HK Tau B having an inclination of $i = 84°$ (Villenave et al. 2020). Therefore, we list their inclinations together in the table and treat them as an uncertainty in our result comparison in the later sections.

2.2. TESS Observations of T Tauri Stars in TMC

TESS is an MIT-led NASA mission launched on 2018 April 18, to search for nearby transiting exoplanets using fast-sampling (2 minutes) time-series data with high photometric precision, which is also well suited for studies of stellar physics. The TMC was in the field of view of TESS in Sectors 43 and 44 from 2021 September 16 to 2021 November 6. Fourteen of our LAMOST CTTS targets have released TESS 2-minute-cadence light-curve data (see Table 1).

There are two kinds of flux information contained in the TESS data: Simple Aperture Photometric (SAP) flux, and the Pre-search Data Conditioning Simple Aperture Photometric (PDCSAP) flux. The SAP flux is produced by summing the count rates of the pixels within a customized aperture given by

Table 2
Stellar Properties of 16 CTTSs in This Study

Name	Radius ($R_\odot$)	Mass ($M_\odot$)	Spec. Type	Distance (pc)	Inclination (deg)
(1)	(2)	(3)	(4)	(5)	(6)
AA Tau	1.72	0.55	M0.6	134.671	59.1 ± 0.3
BP Tau	1.30	0.63	M0.5	127.398	38.2 ± 0.5
CI Tau	1.53	0.90	K5.5	160.318	50.0 ± 0.3
DL Tau	1.20	0.94	K5.5	159.936	45.0 ± 0.2
DN Tau	2.05	0.55	M0.3	128.601	35.2 ± 0.5
DQ Tau	1.77	0.54	M0.6	195.381	16.1 ± 1.2
FN Tau	2.30	0.29	M3.5	129.894	20.0 ± 10.0
GG Tau	2.39	0.63	K7.5	116.395	37.0 ± 1.0
GO Tau	1.25	0.41	M2.3	142.383	53.9 ± 0.5
Haro 6-13	1.83	0.84	K5.5	128.555	41.1 ± 0.3
HK Tau*	1.36	0.49	M1.5	140.000	56.9(HK Tau A), 84.0 (HK Tau B)
HL Tau	7.00	1.70	K3	140.000	47.0 ± 0.4
IQ Tau	1.55	0.51	M1.1	131.511	62.1 ± 0.5
UY Aur	1.90	0.70	K7.0	152.279	42.0
GI Tau	1.72	0.58	M0.4	129.436	43.8 ± 1.1
HP Tau	1.81	1.06	K4.0	171.248	18.3 ± 1.3

Note. The masses and radii of most CTTSs are provided in Herczeg & Hillenbrand (2014), with the exception of HL Tau. The radius ($R = 7\,R_\odot$) and mass ($M = 1.7\,M_\odot$) of HL Tau are given by Liu et al. (2017) and Pinte et al. (2016), respectively. The spectral types are obtained from the LAMOST spectral pipeline. The distances are from the parallax measurements reported in Gaia Collaboration (2020). The references of the inclinations are as follows: BP Tau, CI Tau, DL Tau, DN Tau, DQ Tau, GO Tau, Haro 6-13, IQ Tau, GI Tau, and HP Tau (Long et al. 2019); HL Tau (Partnership et al. 2015); AA Tau (Loomis et al. 2017); GG Tau (Guilloteau et al. 1999); HK Tau A (Manara et al. 2019) and HK Tau B (Villenave et al. 2020); UY Aur (Close et al. 1998). Note that the stellar parameters, mass and radius, of HK Tau shown here belong to HK Tau A.

the Science Processing Operations Center (SPOC) pipeline (Jenkins et al. 2016). The SAP flux is often affected by systematic errors such as long-term trends, which have been removed from the PDCSAP flux using co-trending basis vectors. Therefore, the PDCSAP flux is often cleaner than the SAP flux. In this study, we use the PDCSAP flux data with good quality (flag bits QUALITY = 0) in our analyses. Although the long-term trends might be the true signal of the stars, the unsteady accretion flows have relatively short timescales and should not be affected significantly by removing the long-term trend signal.

Considering the large size of the TESS pixel scale ($21'' \times 21''$), the contamination due to the nearby sources in crowded regions may be unavoidable. To investigate whether the light curves of our targets of interest are contaminated by the neighboring stars, the Python package Lightkurve (Lightkurve Collaboration et al. 1812) was employed. We downloaded the target pixel file (TPF) of each star and plotted it together with the coordinates of the field stars with G_{RP} mag < 15 queried from Gaia DR3 (Gaia Collaboration 2020). The left panel of Figure 2 is an example, the TPF of GG Tau (TIC 245830955). The pink mask region is the SPOC pipeline aperture, the red open circles are the locations of the field stars, and GG Tau is marked by a red filled circle. In addition to GG Tau, there is one neighboring star within the SPOC aperture. The neighbor star ($G_{RP} \sim 13$) is much fainter than GG Tau ($G_{RP} \sim 10$). In addition, the overall shapes of the light

curves extracted using various test apertures do not change significantly compared to the light curve from the SPOC aperture. As a result, the SPOC-given PDCSAP flux of GG Tau is reliable for the following research. The right panel of Figure 2 shows another example, GI Tau (TIC 268444803). There are three neighbor stars within or at the edge of the SPOC aperture of GI Tau. One of them is GK Tau ($G_{RP} = 10.89$) and is about equally bright to GI Tau ($G_{RP} = 11.5$). After the examination with different test apertures, we found that it is impossible to distinguish the variability feature between GI Tau and the field stars in the light curve. Therefore, the GI Tau data were excluded from the following analysis. In the same way, HL Tau has a similar problem to GI Tau and was also excluded. Ultimately, there were only 12 targets for which the data could be used in the subsequent analyses.

3. Analysis

3.1. Calibrating Relative Flux of LAMOST Data to Absolute Units

Due to the limited number of spectral standard stars in the LAMOST survey, no absolute flux-corrected data are available; only relative flux-corrected data can be used. To obtain the physical flux information, we adopt the template spectra of weak-line T Tauri stars (WTTSs) with spectral type ranging from K5 to M7 provided by Manara et al. (2013). We first normalize the template spectra and LAMOST spectra using the mean flux between 7750 and 8000 Å because this range has relatively few emission/absorption features. In this way, we find the best-fit template spectra with the corresponding spectral types for every LAMOST spectra. We then convert the normalized flux of the template spectra and LAMOST spectra back to the physical flux level of template spectra before normalization. Finally, the absolute calibrated flux density of LAMOST data ($F_{\lambda,\mathrm{cal}}$) is obtained by using the following equation:

$$F_{\lambda,\mathrm{cal}} = F_{\lambda,\mathrm{tem}}\left(\frac{d_2}{d_1}\right)^2, \qquad (1)$$

where $F_{\lambda,\mathrm{tem}}$ is the flux density of the best-fit template spectra, d_2 is the distance in parsecs of the template star given by Manara et al. (2013), and d_1 is the distance in parsecs of our sample.

To ensure the accuracy of our calibrated absolute flux measurements, we have cross-checked our results with photometric data obtained by ASAS-SN (Jayasinghe et al. 2018, 2019) and Pan-STARRS (Chambers et al. 2016; Flewelling et al. 2020) surveys if any, which were taken within 20 days of the LAMOST observation date. As CTTSs are known to be highly variable stars, this additional step provides further validation of our flux calibration. In these surveys, we have identified the following stars in our samples with the photometric data that meet the criteria: (1) from ASAS-SN, AA Tau in the SDSS g band and BP Tau in the V band; (2) from Pan-STARRS SDSS g band, DL Tau, DN Tau, Haro 6-13, HL Tau, and IQ Tau; and (3) from Pan-STARRS SDSS i band, GO Tau and HK Tau. The flux (in mJy) and observation date (in MJD) of these photometric data are listed in Table 3. We convert the flux units of the survey photometric data from mJy to the same units as our calibrated LAMOST spectra. Next, we scale the calibrated LAMOST
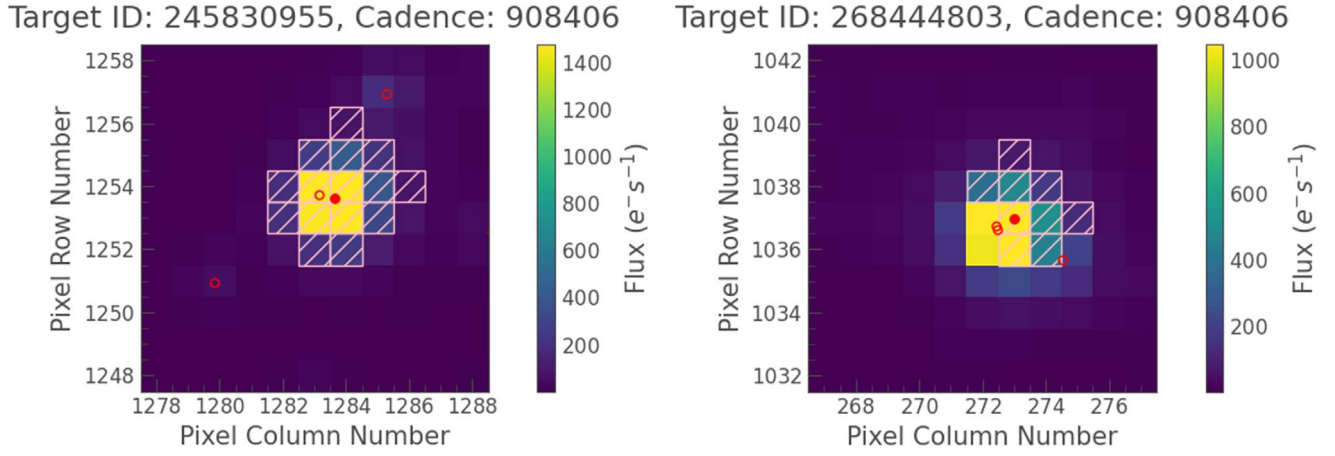
Figure 2. The example for demonstrating the examination of the contamination from nearby sources. The left panel is the TPF of GG Tau (TIC 245830955), and GG Tau is marked by a red filled circle. The red open circles are the field stars with $G_{RP} < 15$ queried from Gaia DR3. The pink mask pixels are the aperture given by the SPOC pipeline. We found that the field star located in the aperture is much fainter than GG Tau, and the overall shapes of light curves from different test apertures do not change significantly compared to the SPOC light curve. Therefore, we verified that the data of GG Tau can be used in this study. The right panel is the TPF of GI Tau (TIC 268444803). There are three neighbor stars within or at the edge of the SPOC aperture, and one of them is equally bright to GI Tau, making it hard to distinguish the variability feature between GI Tau and the neighbor stars in the light curve. As the result, we excluded GI Tau data from the following analysis.

Table 3
Photometric Data of our Samples Taken by ASAS-SN and Pan-STARRS Surveys within 20 Days of LAMOST Observation

Name	LAMOST OBT (MJD)	ASAS-SN OBT (MJD)	ASAS-SN g (mJy)	ASAS-SN V (mJy)	Pan-STARRS OBT (MJD)	Pan-STARRS g (mJy)	Pan-STARRS i (mJy)
(1)	(2)	(3)	(4)	(5)	(6)	(7)	(8)
AA Tau	58512.516	58512.037	0.88 ± 0.06	...	...	...	...
BP Tau	56682.458	56700.294	...	48.58 ± 0.18	...	...	...
CI Tau	56682.458	57424.345	...	16.49 ± 0.14	...	...	...
DL Tau	56284.592	...	...	...	53600.366	10.37 ± 0.01	...
DN Tau	56284.609	...	...	...	56333.298	26.09 ± 0.02	...
GO Tau	56625.627	...	...	...	56605.593	...	47.64 ± 0.06
Haro 6-13	56284.597	...	...	...	56300.366	1.25 ± 0.01	...
HK Tau	56238.778	...	...	...	56236.566	...	52.60 ± 0.06
HL Tau	56332.471	...	...	...	56333.325	1.57 ± 0.01	...
IQ Tau	56284.607	...	...	...	56300.365	49.00 ± 0.04	...

spectra to match the flux from the surveys at the effective wavelength of the corresponding band. This allows us to obtain a more accurate calibrated flux for our LAMOST data. Figure 3 shows the example spectra of the flux calibration processes of three stars: DL Tau, AA Tau, and GO Tau. For stars that lack survey photometric data, we still use their spectra in the following analysis. However, we note that the results obtained from these data could be uncertain by an order of 0–1.

3.2. Mass Accretion Rate Measurements from LAMOST Spectra Analysis

Using the LAMOST low-resolution spectral data, we are able to estimate the mass accretion rates of T Tauri stars by analyzing various permitted emission lines of Hα $\lambda6563$, Hβ $\lambda4861$, Ca II $\lambda\lambda8498$, 8542, 8662, and He I $\lambda\lambda4471$, 5875, 6678, 7065 (Fang et al. 2009; Herczeg et al. 2009; Alcalá et al. 2014, 2017), which are generated by the accretion flows between the disk and star, in the available wavelength coverage. The emission profiles of these lines in all spectra are shown in Figures 4, 5, 6, and 7.

For each spectrum, we first estimate the equivalent width (EW) of the emissions with the equation

$$\text{EW} = \int \left(\frac{F_\lambda}{F_o} - 1 \right) d\lambda, \quad (2)$$

where F_λ is the spectral flux of the line defined to be within 3σ of the best-fit Gaussian model with the central wavelength of the particular line; F_o is the average flux of the continuum in the same range. The EWs of all available emissions in the spectra are listed in Table 5. Then, the emission's flux (F_{em}) and luminosity (L_{em}) can be obtained using the following equations:

$$F_{em} = \text{EW}_{em} F_c(\text{em}), \quad (3)$$

$$L_{em} = 4\pi d^2 F_{em}. \quad (4)$$

Here EW_{em} represents the EW of the emission, $F_c(\text{em})$ is the local continuum flux in the emission's wavelength range, and d is the distance to the stars. The mass accretion luminosity (L_{acc}) of a T Tauri star can be determined from the line luminosity (L_{line}) by using

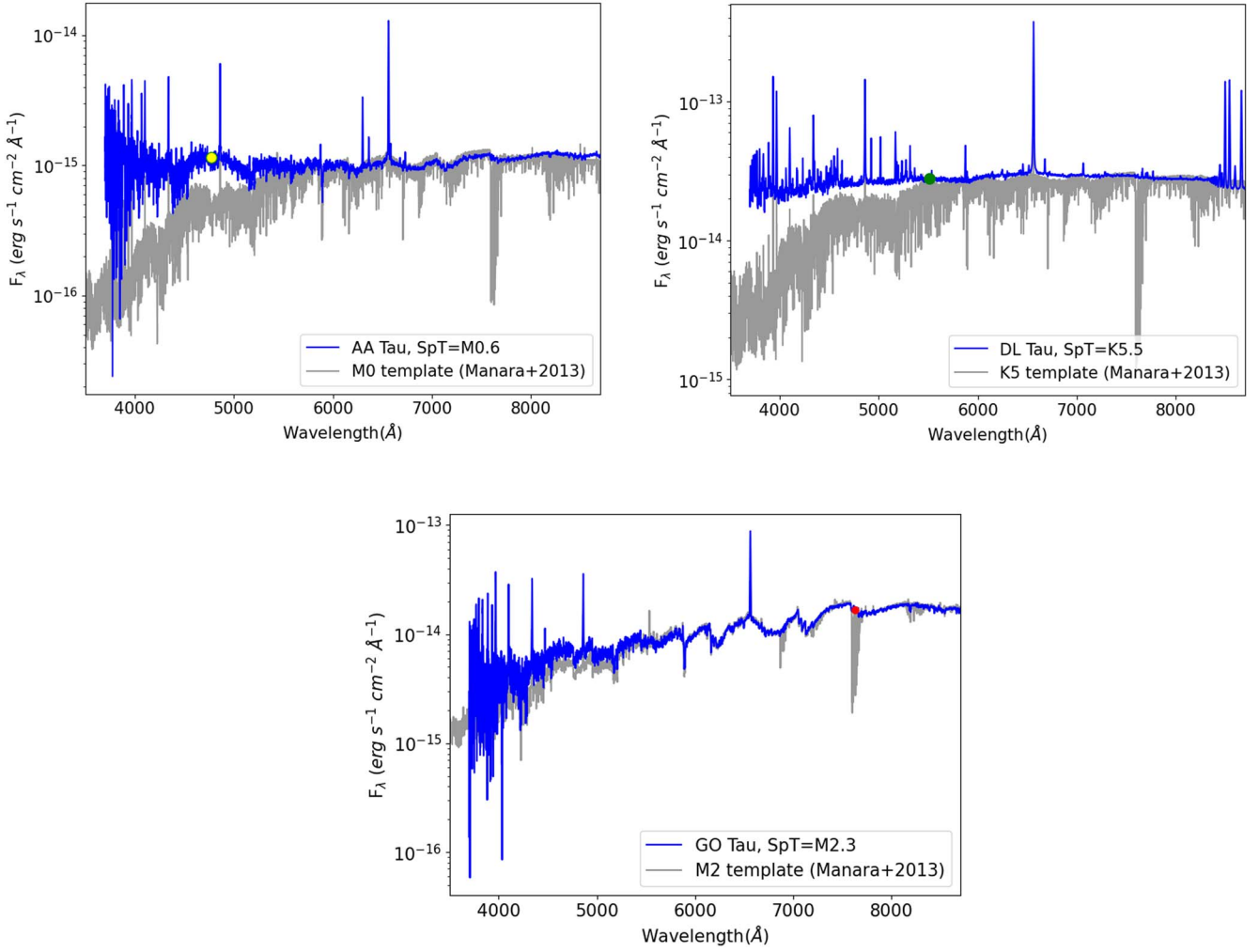$$\log(L_{acc}/L_\odot) = b + a^*\log(L_{line}/L_\odot), \quad (5)$$

Figure 3. Three examples of the flux calibration processes in this study. The top left panel is AA Tau, the top right panel is DL Tau, and the bottom panel is GO Tau. In each panel, the blue curve represents the star's spectrum, while the gray curve represents its corresponding best-fit template spectrum given by Manara et al. (2013). The photometric data from ASAS-SN g band and V band are marked as a yellow circle in the AA Tau case and a green circle in the DL Tau case, respectively. The Pan-STARRS i-band data of GO Tau are marked as a red circle in the GO Tau panel.

where $L_\odot$ is the solar luminosity. The coefficients a and b of every line used in the study are given by Alcalá et al. (2017, see Tabel B.1. in their paper).

If the accretion energy is reprocessed fully into the accretion continuum, $L_{\rm acc}$ can be converted into the mass accretion rate ($\dot{M}_{\rm acc}$) using the following equation from Herczeg & Hillenbrand (2008):

$$\dot{M}_{\rm acc} = \frac{L_{\rm acc} R_*}{GM_* \left(1 - \frac{R_*}{R_{\rm in}}\right)}, \tag{6}$$

where M_* is the stellar mass, G is the gravitational constant, R_* is the stellar radius, and $R_{\rm in}$ is the inner radius of the disk, which is defined as the disk truncation radius of CTTSs, with a standard value of $5R_*$ (Gullbring et al. 1998). The estimated mass accretion rates from all available emissions are displayed in Table 6.

3.3. Variability of Our CTTS Sample

A statistical metric system reported by Cody et al. (2014) allows the light curves of young stellar objects to be classified into different categories; thus, it is useful to recognize the burst-like accretion events in the TESS light curves of our samples. The system contains two metrics: the flux asymmetry (denoted as M), and the quasi–periodicity (denoted as Q). The metric M is the first one we focus on here, which represents the light-curve behavior tendency of dipping ($M > 0$) and bursting ($M < 0$). We determine the metric M following the approach explained in detail by Cody & Hillenbrand (2018, see Section 5 in their paper). We first normalize the light curve with the median of the flux and smooth it using a 200 point moving mean. After subtracting the smoothed light curve from the original one, we identify the 5σ outliers in the residual curve and remove their counterparts from the original curve. Then, the metric M is estimated using the formula

$$M = -(f_{5\%} - f_{\rm med})/\sigma_f, \tag{7}$$

where $f_{5\%}$ is the mean of the first and last 5% of the fluxes in the outlier-free curve, and $f_{\rm med}$ and σ_f are the median flux and the rms of the original curve, respectively. Stars with $M < -0.25$ are likely to display the accretion-like burst variability in their light curves.
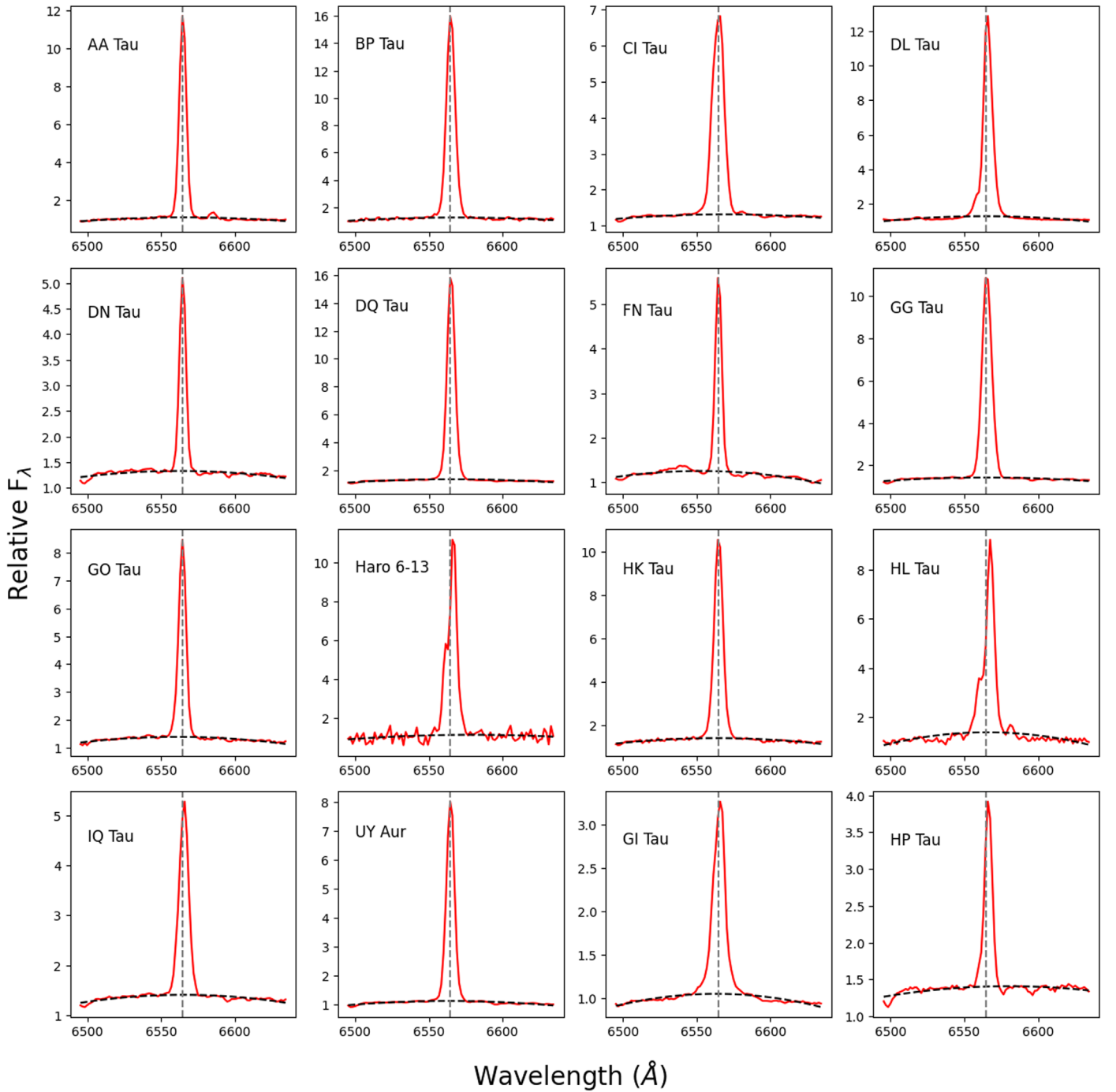
Figure 4. Hα emission profiles of our targets observed by LAMOST. In each panel, the spectra are displayed in red, and the black line represents the fit local continuum. The dashed vertical line in gray marks the center wavelength of the Hα line.

The second metric Q is used to evaluate periodicity tendency of light curves in the range from $Q = 0$ (purely periodic) to $Q = 1$ (stochastic) (Cody et al. 2014). To determine the Q values of the light curve, we first fold up the light curves with the associated periods reported by Percy et al. (2010) and Rebull et al. (2020) if any. One special case is DQ Tau, which is a spectrocopic binary and has two reported brightness variation periods: $\sim$15.8 and $\sim$3.03 days. The first one is attributed to the brightening effect associated with mass accretion and magnetic reconnection that occurs around the periastron when two stars approach each other (Mathieu et al. 1997; Salter et al. 2010; Czekala et al. 2016;

Getman et al. 2016). The second one is the rotational modulation caused by the presence of the spots, and we use it to determine the Q value for DQ Tau. Since the morphologies of variability in young stellar objects could vary with time (e.g., Sousa et al. 2016), we manually examine the phase curve to ensure the validity of the reported periods for our data. If the star has no reported period, or if the reported period is not applicable to our data, we redetermine/ determine the period by, first, identifying the maximum in the autocorrelation function and, second, refining the period within the full width at half maximum (FWHM). The best period solution is determined by selecting the one that
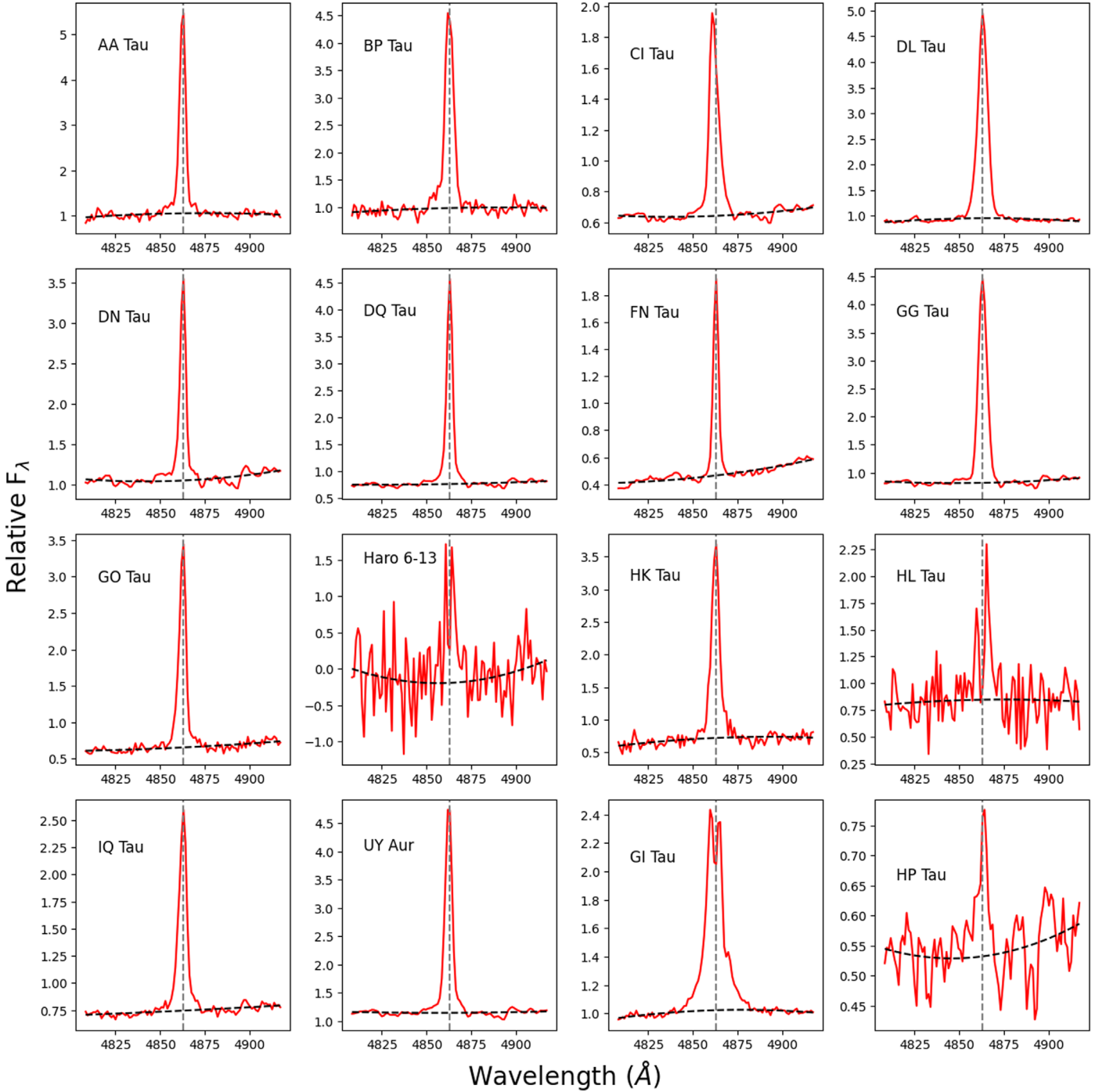
Figure 5. Hβ emission profiles of our targets observed by LAMOST. Dashed vertical gray lines represent the center of the line in each panel.

provides the optimal folded phase curve counterpart. This selection process involves manually examining the phase curves and comparing them to those from other potential period values. Figure 8 illustrates DL Tau and IQ Tau as examples, with estimated periods of 10.4 and 12.9 days, respectively. Next, we use the Gaussian process (GP) to produce a smooth light-curve pattern with the optimal period, which is then subtracted from the original light curve to measure the residual noise. Finally, the resulting residual variance is divided by the variance of the original light curve to obtain the Q value.

We then divide the light curves of our samples into eight different categories using the definition of Q and M ranges given by Cody et al. (2022):

1. Burster (B): $M < -0.25$
2. Purely periodic symmetric (P): $Q < 0.15$ and $-0.25 < M < 0.25$
3. Quasi-periodic symmetric (QPS): $0.15 < Q < 0.85$ and $-0.25 < M < 0.25$
4. Purely stochastic (S): $Q > 0.85$ and $-0.25 < M < 0.25$
5. Quasi-periodic dipper (QPD): $0.15 < Q < 0.85$ and $M > 0.25$
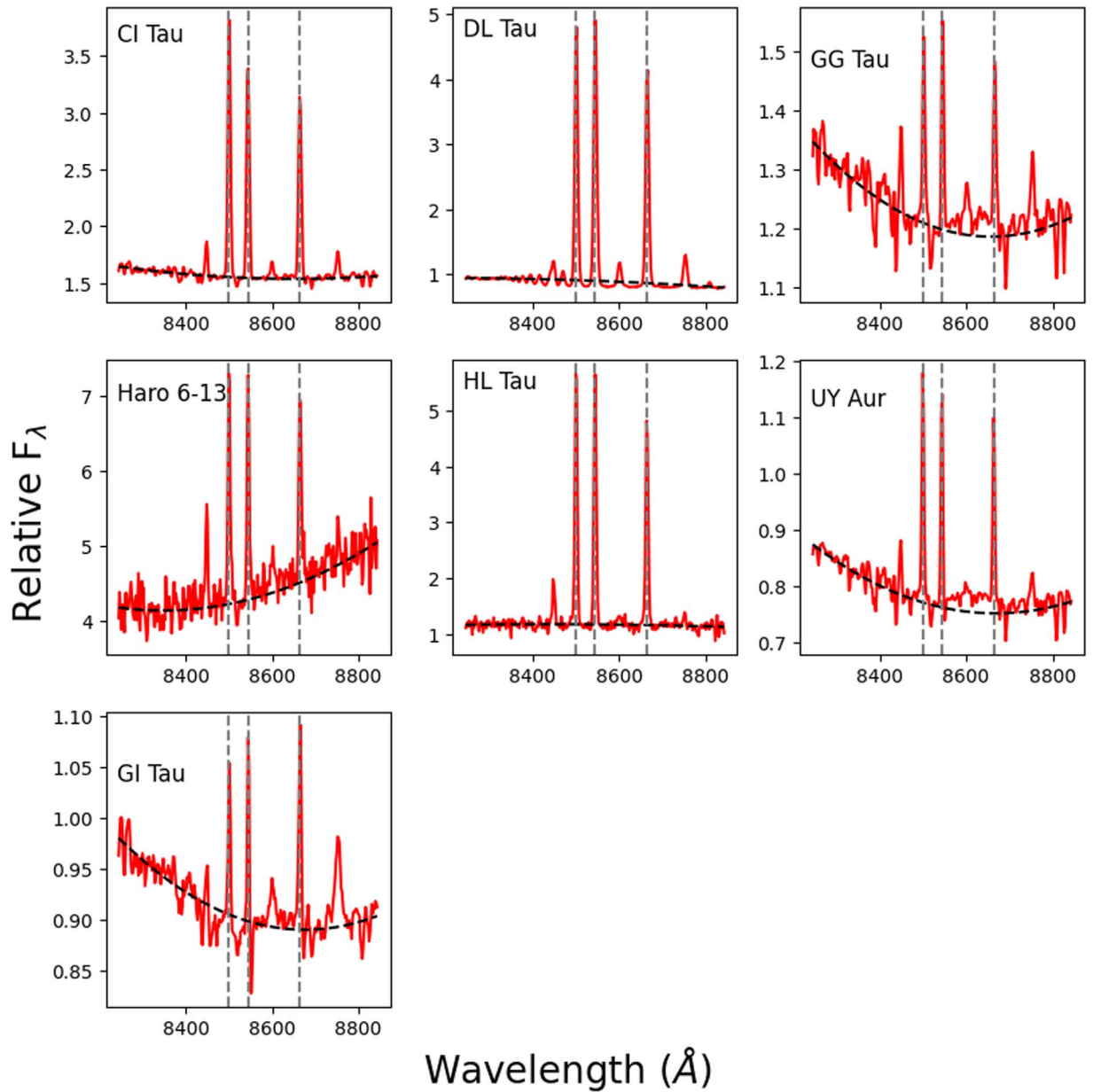
Figure 6. Ca II λλ8498, 8542, 8662 emission profiles of our targets observed by LAMOST. Dashed vertical gray lines represent the center of the Ca II triplet lines in each panel.

6. Aperiodic dipper (APD): $Q > 0.85$ and $M > 0.25$
7. Long timescale (L)
8. Variable but unclassifiable (U)

The values of Q and M for the CTTSs are listed in Table 4, along with the variability classes. The TESS light curves of 12 CTTSs in our sample, along with their assigned M, Q, and variability classes, are shown in Figure 9. Also in Figure 10, we show the distribution of the variability statistics for our sample in the Q–M diagram.

3.4. Mass Accretion Rate Measurements from TESS Light Curves

In Section 3.3, we have identified four bursters in our samples: DQ Tau, DL Tau, GG Tau, and Haro 6-13. To estimate the mass accretion rates from their TESS light curves, we need to first convert the excess flux yields associated with

the bursts in the TESS bandpass to the U-band excess luminosity, which can be used as the proxy for the mass accretion rates (e.g., Tofflemire et al. 2017).

To do so, we searched for other observational data of the stars from ASAS-SN, Pan-STARRS, and ZTF (Bellm et al. 2019; Masci et al. 2019; IRSA 2022) that were taken simultaneously with TESS in different optical bands. We found such data only for DL Tau and Haro 6-13. DL Tau was observed by the ASAS-SN survey and the ZTF survey. A burst event of DL Tau at BT– 2,457,000 = 2504 days was captured by TESS, ZTF g, and ASAS-SN g. Haro 6-13 was observed by the ZTF during the same observation period as the TESS mission for it. A burst event in Haro 6-13's TESS light curve at BT–2,457,000 = 2516 days was also observed by the ZTF with both the g and r bands. Their light curves of the bursts are shown together in Figure 11.

Here the periodic variation due to possible dark spot modulation has been removed from the TESS light curves of
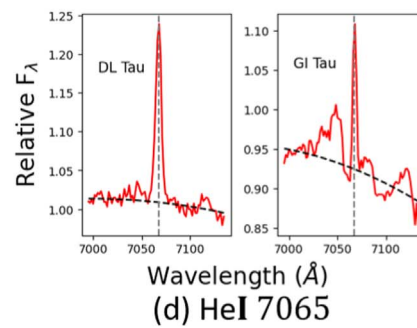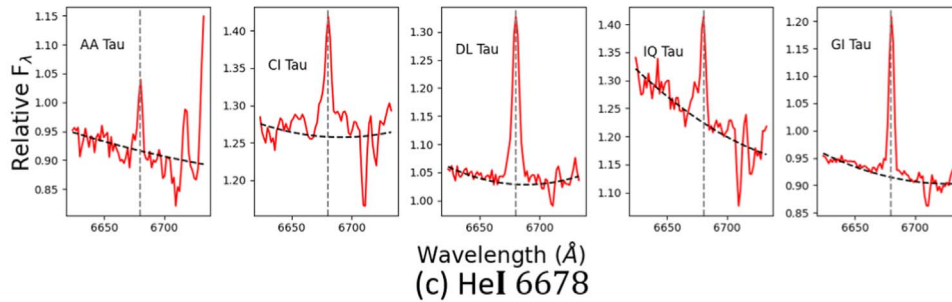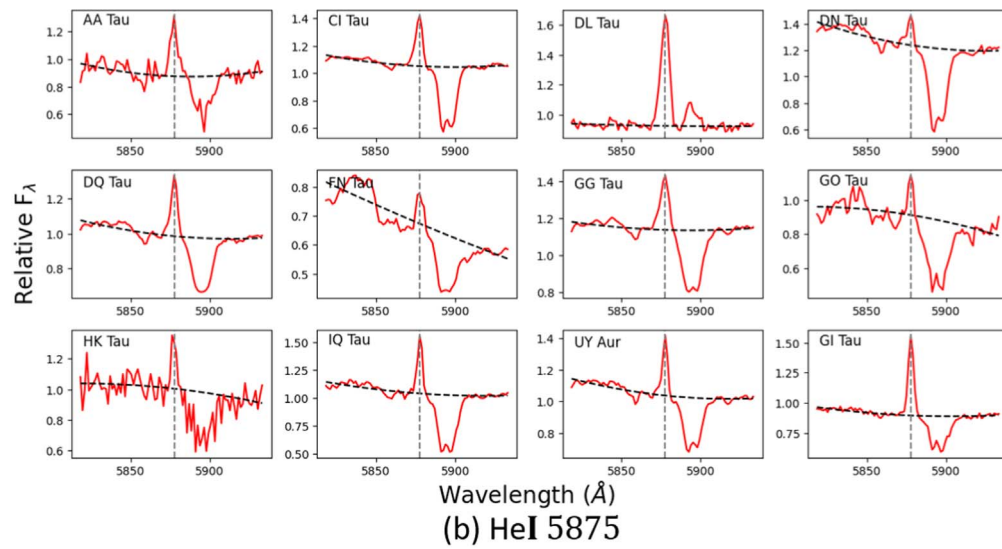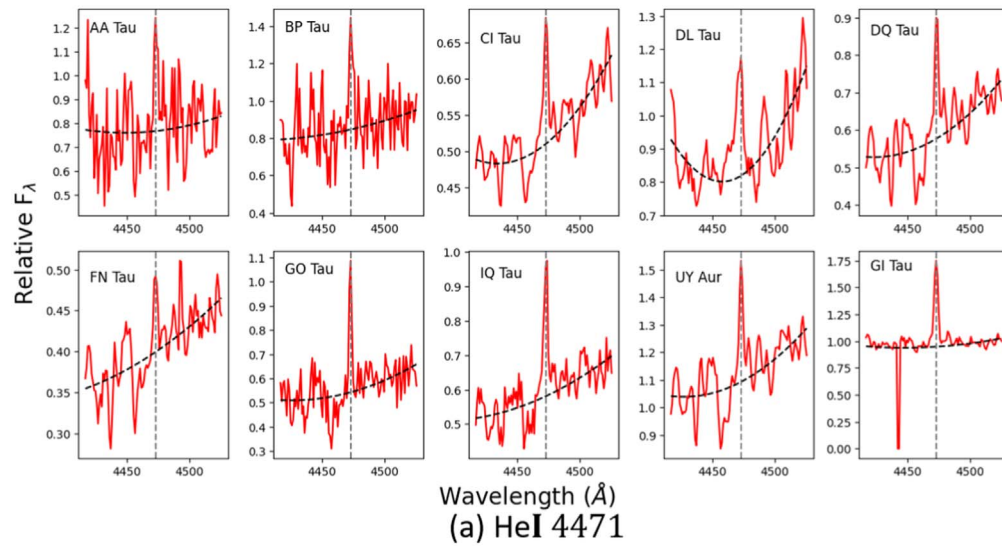
Figure 7. a−dHe I $\lambda\lambda$4471, 5875, 6678, 7065 emission profiles of our targets observed by LAMOST. Dashed vertical gray lines represent the center of He I in each panel.

Table 4
The Photometric Variability Classes of the CTTSs Observed by TESS in This Study and the Literature (If Any)

Name (1)	M^a (2)	M^b (3)	M^c (4)	Q^a (5)	Q^b (6)	Q^c (7)	Variability[a] (8)	Variability[b] (9)	Variability[c] (10)	Period[a] (11)	Period[d] (12)	Period[e] (13)
AA Tau	−0.13	−0.30	...	0.35	1.00	...	QPS	S	...	8.3	8.2	...
BP Tau	−0.03	...	−0.03	0.81	...	0.83	QPS	...	QPS	7.6	7.6	...
DL Tau	−0.63	...	...	0.72	...	...	B	...	...	10.4	9.35	...
DN Tau	−0.23	...	...	0.17	...	...	QPS	...	...	6.18	6.1	...
DQ Tau	−1.14	−0.87	...	0.98	0.54	...	B	B	...	3.03	...	3.03
FN Tau	−0.09	...	0.03	0.85	...	0.60	QPS	...	QPS	7.33	...	8.77
GG Tau	−0.32	...	...	0.64	...	...	B	...	...	10.3	10.3	...
GO Tau	0.61	0.25	...	0.88	0.90	...	APD	U	...	2.51	...	...
Haro 6-13	−0.31	0.10	...	0.85	0.92	...	B	S	...	3.27	...	3.27
HK Tau	0.33	0.11	...	0.27	0.72	...	QPD	QPS	...	3.31	3.31	...
IQ Tau	0.08	−0.13	...	0.05	0.78	...	P	QPS	...	12.92	...	6.67
UY Aur	0.08	...	−0.49	0.74	...	0.74	QPS	...	B	3.04	...	...

Notes. The units of the period are days.
[a] Represents the measurements given in this study.
[b] Cody et al. (2022).
[c] Robinson et al. (2022).
[d] Percy et al. (2010).
[e] Rebull et al. (2020).

DL Tau and Haro 6-13 by subtracting the best-fit sinusoidal curves with corresponding periods (see Table 4) from the original curves. The fluxes of both data have good-quality flags, and both are normalized to their respective median flux levels using the equation

$$\frac{\Delta F}{\tilde{F}} = \frac{F - \tilde{F}}{\tilde{F}}, \tag{8}$$

where F represents the flux as a function of time and $\tilde{F}$ is their median in the light curve. We express the observed amplitude due to the hot spot associated with the accretion burst, which covers an area $A = X\pi R_*^2$ on the visible stellar photosphere, where X is the filling factor and R_* is the stellar radius, as

$$\left(\frac{\Delta F}{\tilde{F}}\right)_\lambda = X\frac{\int B_\lambda(T_{\mathrm{hspot}})R_\lambda d\lambda}{\int B_\lambda(T_*)R_\lambda d\lambda} = X\frac{T_{\mathrm{hspot}}^4 f_\lambda(T_{\mathrm{hspot}})}{T_*^4 f_\lambda(T_*)}, \tag{9}$$

where B_λ is the Planck function, R_λ is the transmission function of the band, T_* is the stellar effective temperature, and T_{hspot} is the temperature of the hot spot. The integral term can be expressed as $\sigma T^4 f_\lambda(T)$, where σ is the Stefan–Boltzmann constant and f_λ is the bandpass response factor as a function of temperature for the used band (λ). The response factor functions of the bands used in the study, i.e., SDSS g, ZTF g, ZTF r, U, and TESS bands, are shown in Figure 12. The amplitudes of DL Tau's event are 0.848, 0.77, and 0.438 in ASAS-SN's SDSS g, ZTF g, and TESS bands, respectively. We note that since there are two data points from ZTF g obtained during the event, the reported amplitude in ZTF g is computed as the mean value of these data points. Additionally, the central time between these two data points is very close to that of ASAS-SN's observation. With this information, we can estimate the temperature of the hot spot by using the following equation:

$$\frac{(\Delta F/\tilde{F})_{\lambda 1}}{(\Delta F/\tilde{F})_{\lambda 2}} = \frac{f_{\lambda 1}(T_{\mathrm{hspot}})f_{\lambda 2}(T_*)}{f_{\lambda 2}(T_{\mathrm{hspot}})f_{\lambda 1}(T_*)}. \tag{10}$$

The hot spot's temperatures derived from TESS–ASAS-SN g and TESS–ZTF g are about 5700 and 5500 K, respectively. As a result, the temperature of the hot spot is estimated to be the average of these values, which is approximately 5600 K. We substitute this value back into Equation (9) to calculate the filling factor of the spot and obtain $X = 0.038$ or 3.8%.

For the case of Haro 6-13, the burst amplitudes in TESS, ZTF r, and ZTF g bands are measured to be 0.292, 0.4, and 0.75, respectively. Because there is approximately a 0.1-day timing gap between the ZTF g and ZTF r data, the amplitude in the TESS band is the average of the corresponding amplitudes at ZTF g and ZTF r data times. By following the same estimation procedure as we conducted for DL Tau's burst, the temperature of Haro 6-13's burst is estimated to be 7100 K based on TESS and ZTF g-band data. The estimated temperature becomes a bit hotter when using TESS and ZTF r-band data, 7715 K. Thus, we determined the burst temperature of Haro 6-13 to be about 7300 K by averaging these values. The filling factor of the burst-driven hot spot on Haro 6-13 is about $X = 0.008$, or 0.8%. The resulting values of the hot spot temperature and fractional area fall within the range of values observed and modeled in previous studies (e.g., Manara et al. 2013; Venuti et al. 2015), demonstrating the reliability of our method. However, we note that our estimations are lower limits, as we have not considered the limb darkening in Equations (9) and (10). In other words, we assume that the hot spot is located at the center of the visible photospheric disk of the star.

We then extrapolate the burst amplitudes in the U band with the estimated hot spot temperatures and the fractional areas. We find that the burst amplitudes in the U band are about 3.49 and 7.6 times higher than those in the TESS band for DL Tau and Haro 6-13, respectively. We produce the U-band excess amplitude curves of DL Tau and Haro 6-13 by multiplying their normalized TESS light curves by the factors of counterparts. The U-band apparent magnitudes of DL Tau and Haro 6-13 are 14.04 (Ducati 2002) and 19.22 (Audard et al. 2007), which can be converted to flux units of $F_U = 3.77 \times 10^{-11}$ erg s^{-1} cm^{-2} and $F_U = 3.19 \times 10^{-13}$ erg s^{-1} cm^{-2}, respectively. The U-band luminosities,
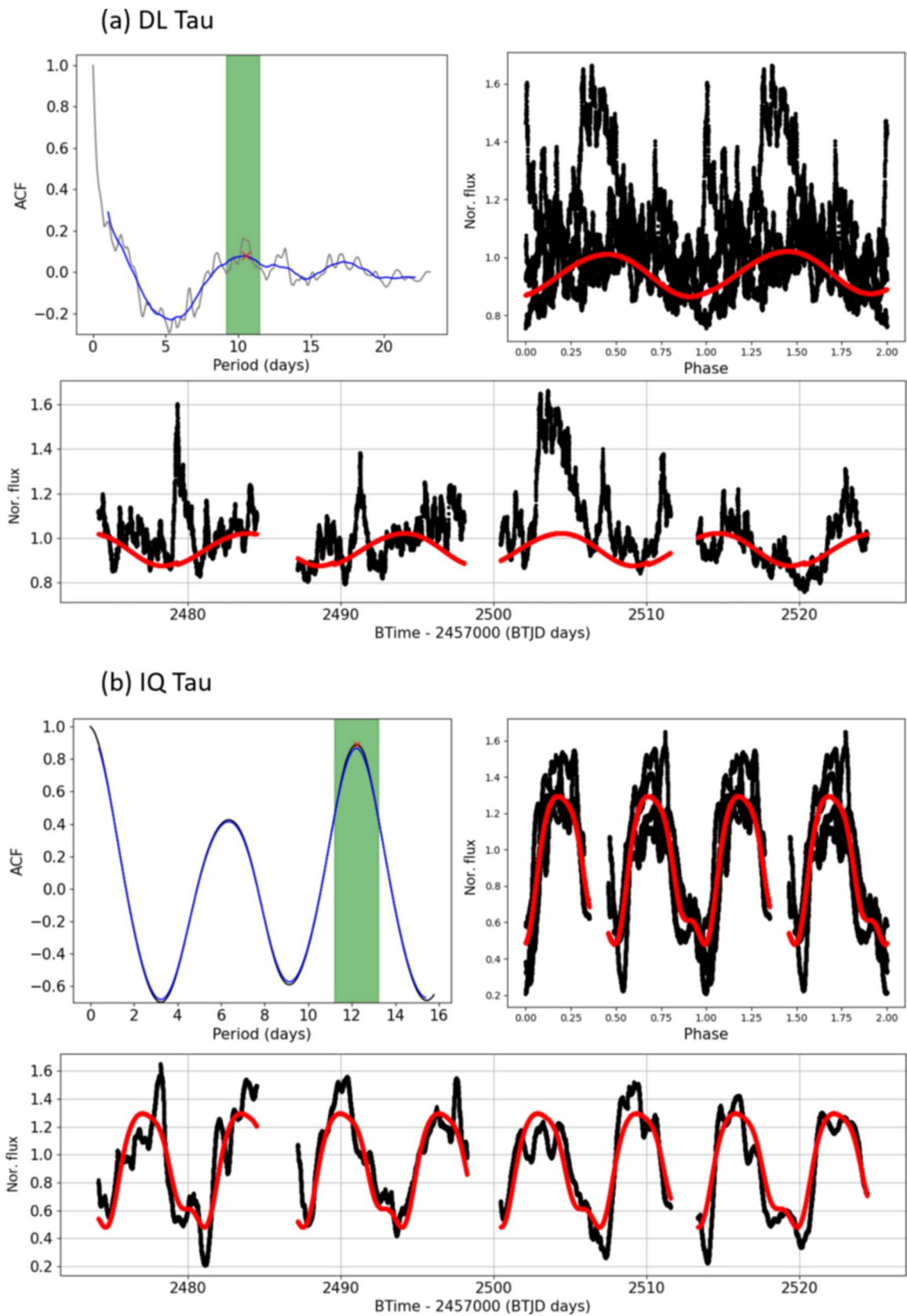
Figure 8. The examples of the period reestimate/estimate of the CTTSs, here showing (a) DL Tau and (b) IQ Tau. In each case, the top left panel shows the autocorrelation function. The gray one is the original ACF, and the blue one is a smoothed version of the ACF. The red cross marks the peak of the ACF, and the FHWM is highlighted by green, from where the best period is determined. The top right panel is the phase curve (black) and the best GP fit curve (red). The panel at the bottom is the full TESS Section 43 and 44 light curve of the star (black) with the best GP fit curve (red). The best periods we found for DL Tau and IQ Tau are 10.4 and 12.9 days, respectively.
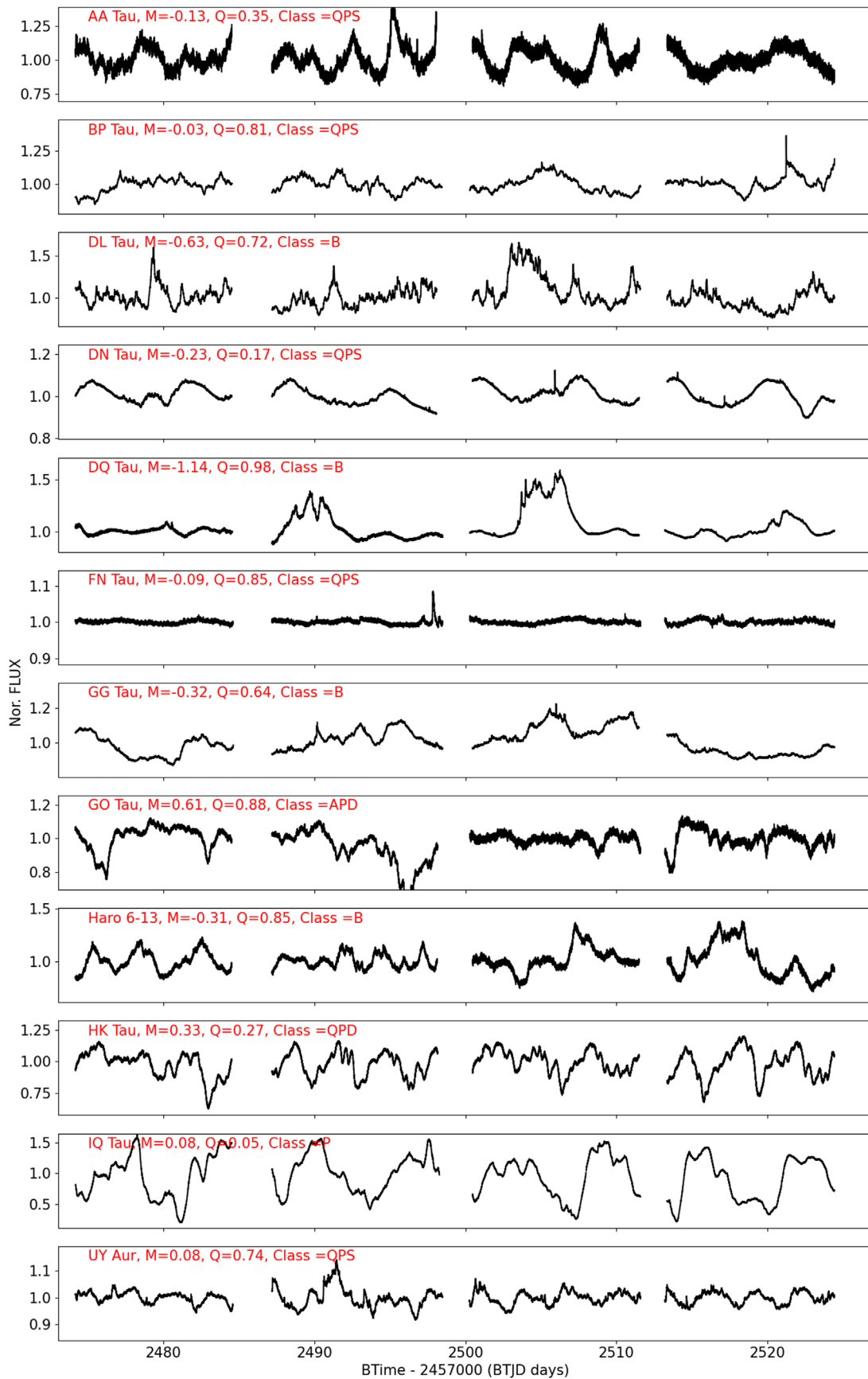
Figure 9. The TESS light curves of 12 CTTSs in our sample. Their variability classes are also displayed.
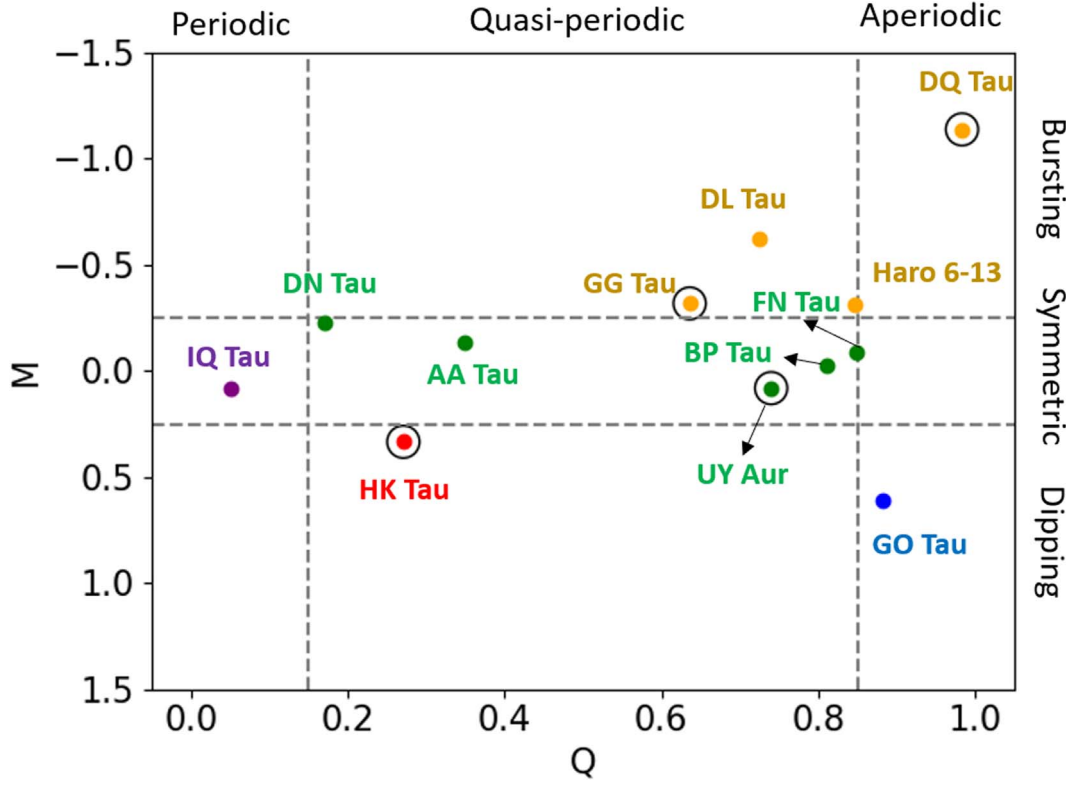
Figure 10. The *Q–M* statistics diagram for our sample of CTTSs. The stars surrounded by black open circles in this diagram are binary or multistar systems. Different colors represent different variability classes: yellow (B), purple (P), green (QPS), blue (APD), and red (QPD).
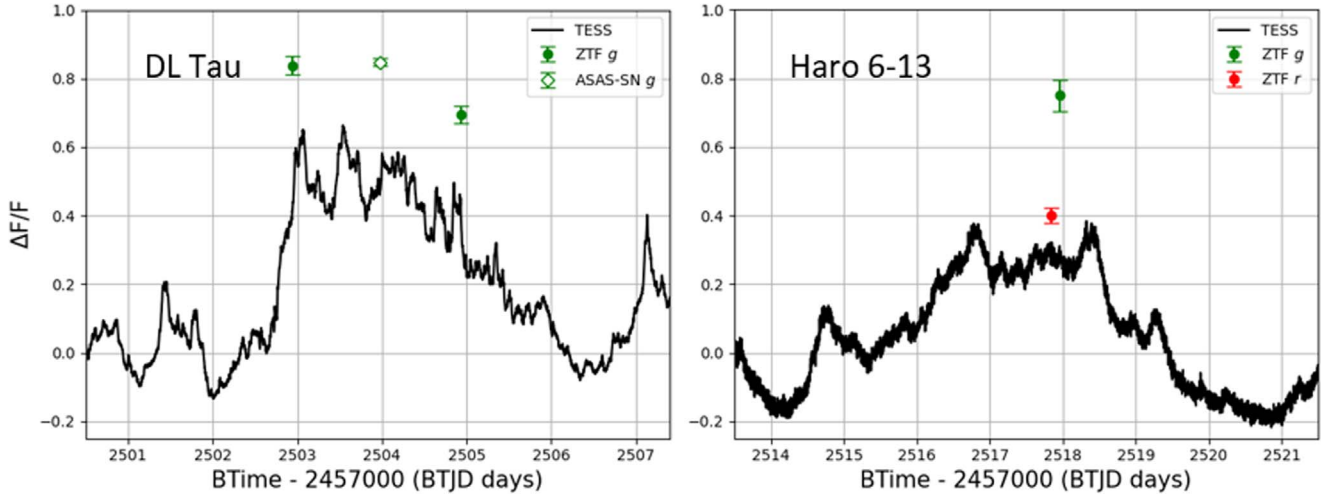
Figure 11. Left panel: a burst event of DL Tau at BT–2,457,000 = 2504 was captured by TESS, ASAS-SN *g*, and ZTF *g*. Right panel: a burst event of Haro 6-13 at BT–2,457,000 = 2516 was observed by TESS, ZTF *g*, and ZTF *r*. In each panel, the black curve represents the burst event observed by TESS, and the green filled circles are *g*-band observations from the ZTF survey. The green open diamond represents the data from the ASAS-SN survey. In the case of Haro 6-13, the red filled circle represents the observation from the ZTF *r* band.

$L_U = 1.15 \times 10^{32}$ erg s^{-1} and $L_U = 6.32 \times 10^{29}$ erg s^{-1}, of DL Tau and Haro 6-13 can be estimated using the formula $L_U = F_U A \pi d^2$, with the distance information of $d = 159$ pc and $d = 129$ pc (Gaia Collaboration 2020). We produce the *U*-band excess luminosity (L_{Uexcess}) curves of these stars by multiplying their *U*-band excess amplitude curves by the L_U values. Then, the accretion luminosities (L_{acc}) can be calculated using an empirical correlation between L_{acc}

and L_{Uexcess} given by Gullbring et al. (1998):

$$\log(L_{\text{acc}}/L_\odot) = 1.09 \log(L_{\text{Uexcess}}/L_\odot) + 0.98, \quad (11)$$

where $L_\odot$ is solar luminosity. Finally, the mass accretion rates can be determined from the accretion luminosities by using Equation (6) with the stellar parameters in Table 2. The mass
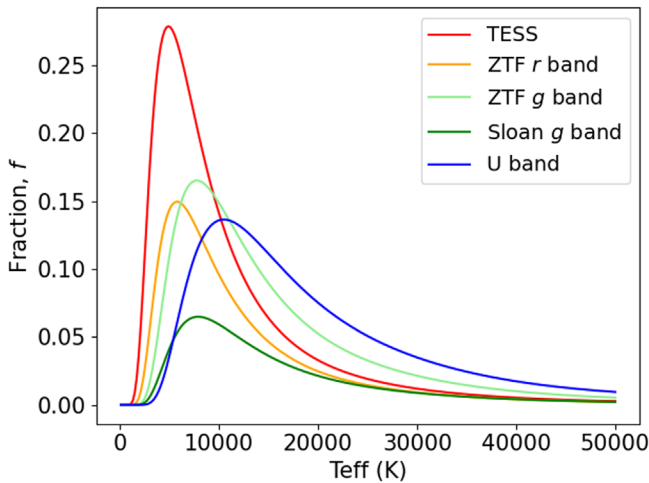
Figure 12. The fractional response functions of TESS (red), ZTF *r* (orange), ZTF *g* (lightgreen), SDSS *g* (green), and *U* bands (blue). They are the function of the blackbody temperature.

accretion rates and luminosities of DL Tau and Haro 6-13 are displayed in Figure 13.

4. Results and Discussion

4.1. Mass Accretion Rates from the LAMOST Spectra

We estimated the mass accretion rates of low-mass CTTSs with spectral types from mid-M to late K in the TMC using LAMOST spectral data. The indicators we used were the Hα λ6563, Hβ λ4861, Ca II $\lambda\lambda$8498, 8542, 8662, and He I $\lambda\lambda$4471, 5875, 6678, 7065 emissions. The EWs of these lines and the corresponding mass accretion rates are listed in Tables 5 and 6, respectively.

All of our samples have the $\dot{M}_{acc}$ measurement estimated from the Hα line. On average, these stars have an Hα mass accretion rate of $1.76 \times 10^{-9} M_\odot \, \mathrm{yr}^{-1}$. GG Tau has the highest measured Hα mass accretion rate among the sample, with a value of $6.35 \times 10^{-9} M_\odot \, \mathrm{yr}^{-1}$. HP Tau has a significant Hα emission, but its mass accretion rate is lower than those of the other stars, with a value of $7.88 \times 10^{-11} M_\odot \, \mathrm{yr}^{-1}$ in this study. On the other hand, from Hβ emissions, the average rate of these stars is $2.89 \times 10^{-9} M_\odot \, \mathrm{yr}^{-1}$. UY Aur and GG Tau both have the highest Hβ-derived rate of $9.11 \times 10^{-9} M_\odot \, \mathrm{yr}^{-1}$. Consistent with the H$\alpha$ result, HP Tau exhibits the lowest mass accretion rate estimated from the Hβ line, which is $2.44 \times 10^{-11} M_\odot \, \mathrm{yr}^{-1}$. Only Haro 6-13 has no Hβ accretion rate because it is too faint for LAMOST in the blue wavelength part, making it impossible to estimate. Not all targets in our sample have measurable EWs for the other emission lines, which means that not all corresponding mass accretion rates could be estimated. Figure 14 shows the mass accretion rate distribution of our targets by displaying the measurements derived from all available emissions adopted in this study. HL Tau has the largest dispersion of the spectral-derived mass accretion rates with a coefficient of variation (CV) value (the ratio of the standard deviation to the mean) of 1.15, as compared to other stars in the sample. The CVs of other stars are smaller than one with a mean value of 0.41 ± 0.22. After field checking, we have ruled out the possibility of contamination from the closest neighboring star of HL Tau, XZ Tau, as it is located about 23″ away from HL Tau and thus can be resolved separately by the LAMOST fiber with a 3.″3

diameter. The underlying mechanism responsible for this phenomenon remains unknown, making it an intriguing topic for future investigation. On the other hand, the lowest-dispersion CV value is found in FN Tau, which is 0.08.

4.2. Mass Accretion Rates of DL Tau and Haro 6-13 from the TESS Light Curves

The time-series mass accretion rates and luminosities derived from the TESS light curves for DL Tau and Haro 6-13 are shown in Figure 13. We find that the mass accretion rate of DL Tau reached up to $2.5 \times 10^{-8} M_\odot \, \mathrm{yr}^{-1}$ during the observation time. The mass accreted by DL Tau over approximately 50 days is $\approx 3.4 \times 10^{-10} M_\odot$, with an average rate of $\approx 2.5 \times 10^{-9} M_\odot \, \mathrm{yr}^{-1}$. These results are comparable to the mean value of the mass accretion derived from LAMOST for DL Tau, which is $4.6 \times 10^{-9} M_\odot \, \mathrm{yr}^{-1}$ with a standard deviation of $2.5 \times 10^{-9} M_\odot \, \mathrm{yr}^{-1}$. Meanwhile, the maximum mass accretion rate of Haro 6-13 from the TESS observations is $2 \times 10^{-10} M_\odot \, \mathrm{yr}^{-1}$. It accreted mass with a value of about $2.7 \times 10^{-12} M_\odot$ over approximately 50 days, with an average rate of $\approx 2 \times 10^{-11} M_\odot \, \mathrm{yr}^{-1}$. These results are overall lower than the measurement, which is about $1.6 \pm 0.8 \times 10^{-9} M_\odot \, \mathrm{yr}^{-1}$ on average, determined from LAMOST data.

An interesting question is whether the mass increase of T Tauri stars is dominated by long-term, steady mass accretion or by occasional bursts of accretion. First, we need to define a steady accretion rate, and this rate does not change over time. We then calculate the total mass accumulated by the steady rate of the star during the TESS observation. This is compared with the total amount of burst accretion to determine whether the CTTS is dominated by steady status or episodic effect.

Here we take the mean rate obtained from LAMOST emission measurement as the steady rate. Thus, the steady rate of mass accretion of DL Tau is $(4.6 \pm 2.5) \times 10^{-9} M_\odot \, \mathrm{yr}^{-1}$. In this case, DL Tau accumulated masses of $(6.3 \pm 3.4) \times 10^{-9} M_\odot$ through a steady rate over a period of about 50 days. This result is larger than the total mass of $\approx 3.4 \times 10^{-10} M_\odot$ accreted by the stars' burst-like events observed by TESS. Similarly, the steady mass accretion of Haro 6-13 is $(1.6 \pm 0.8) \times 10^{-9} M_\odot \, \mathrm{yr}^{-1}$. This value is about one order higher than the maximum of $2 \times 10^{-10} M_\odot \, \mathrm{yr}^{-1}$ from the TESS observation. Therefore, in this scenario the mass accretion processes of DL Tau and Haro 6-13 are both steady accretion dominant.

4.3. Flare Activity of Our CTTS Sample

CTTSs are also known for their high magnetic activity, which is often manifested in flaring events. Flares with sudden, short-lived increases in brightness are thought to be caused by magnetic reconnection events on the star's surface (Parker 1963; Maehara et al. 2012). The magnetic fields of the CTTS form a large loop connecting the star and circumstellar disk. When the magnetic field lines eventually reconnect, a large amount of energy is released in the form of a huge flare. This kind of flare resulting from the star–disk magnetic interaction could last more than 50,000 s, and it is a characteristic feature of CTTSs while affecting the mass accretion process in some degree (Giardino et al. 2007; López-Santiago et al. 2016; Colombo et al. 2019).

4.3.1. Flare Detection

To analyze the flares in our TESS light curves, we employ an algorithm developed by Lin et al. (2019) that generates a flare-free light curve. We then identify individual flare candidates
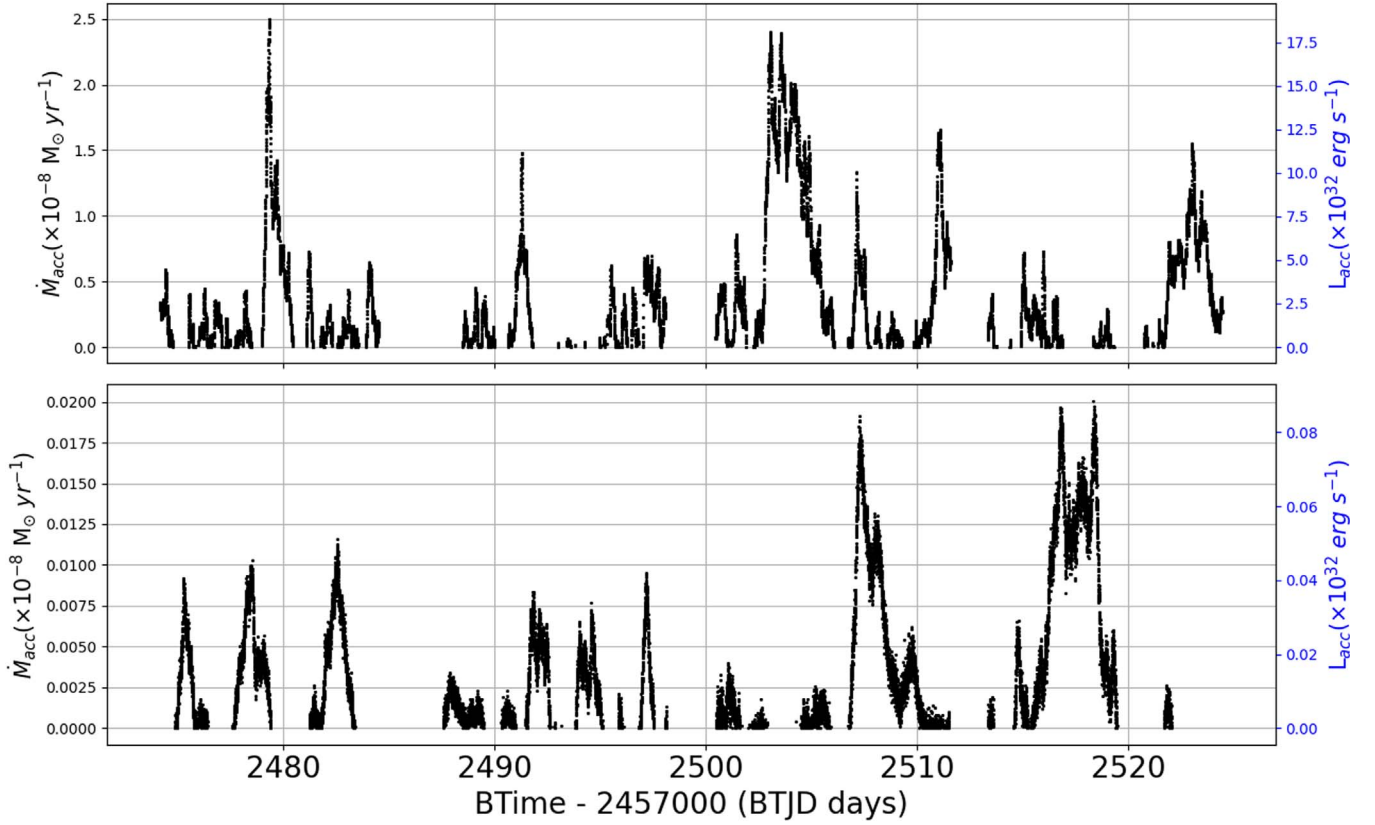
Figure 13. The time-series mass accretion rates of DL Tau and Haro 6-13 are shown in the top and bottom panels, respectively. The left axis shows the mass accretion rates derived from the TESS, ASAS-SN, and ZTF observations, while the right axis displays the corresponding accretion luminosities.

Table 5
Equivalent Widths of All Mass Accretion Indicator Emissions of 16 CTTSs in LAMOST Spectra in This Study

Name (1)	$EW_{H\alpha}$ (2)	$EW_{H\beta}$ (3)	$EW_{Ca\ II8498}$ (4)	$EW_{Ca\ II8542}$ (5)	$EW_{Ca\ II8662}$ (6)	$EW_{He\ I4771}$ (7)	$EW_{HeI5875}$ (8)	$EW_{He\ I6678}$ (9)	$EW_{He\ I7065}$ (10)
AA Tau	66.45 ± 1.16	18.96 ± 0.33	... ± ...	... ± ...	... ± ...	2.14 ± 0.06	3.00 ± 0.07	0.66 ± 0.02	... ± ...
BP Tau	98.29 ± 0.06	23.15 ± 0.01	... ± ...	... ± ...	... ± ...	2.98 ± 0.05	... ± ...	... ± ...	... ± ...
CI Tau	44.39 ± 2.07	13.18 ± 0.61	11.74 ± 0.10	10.18 ± 0.06	8.68 ± 0.01	0.96 ± 0.02	2.17 ± 0.06	0.73 ± 0.04	... ± ...
DL Tau	83.17 ± 0.78	28.41 ± 0.27	40.52 ± 2.43	44.29 ± 0.00	37.03 ± 0.60	2.63 ± 0.08	5.45 ± 0.03	1.92 ± 0.05	1.78 ± 0.03
DN Tau	17.06 ± 0.76	9.70 ± 0.43	... ± ...	... ± ...	... ± ...	... ± ...	0.85 ± 0.05	... ± ...	... ± ...
DQ Tau	81.36 ± 1.31	20.44 ± 0.33	... ± ...	... ± ...	... ± ...	1.89 ± 0.15	1.73 ± 0.11	... ± ...	... ± ...
FN Tau	22.36 ± 0.53	11.57 ± 0.27	... ± ...	... ± ...	... ± ...	0.82 ± 0.00	1.34 ± 0.03	... ± ...	... ± ...
GG Tau	59.92 ± 1.35	26.44 ± 0.60	2.12 ± 0.05	2.08 ± 0.02	1.91 ± 0.06	... ± ...	1.55 ± 0.00	... ± ...	... ± ...
GO Tau	36.64 ± 2.01	20.68 ± 1.13	... ± ...	... ± ...	... ± ...	2.74 ± 0.06	1.73 ± 0.13	... ± ...	... ± ...
Haro 6-13	73.51 ± 1.74	... ± ...	4.97 ± 0.00	4.59 ± 0.00	4.16 ± 0.00	... ± ...	... ± ...	... ± ...	... ± ...
HK Tau	57.27 ± 0.97	25.12 ± 0.42	... ± ...	... ± ...	... ± ...	... ± ...	1.75 ± 0.04	... ± ...	... ± ...
HL Tau	59.73 ± 10.95	10.67 ± 1.96	27.57 ± 0.60	28.72 ± 0.00	24.13 ± 0.29	... ± ...	... ± ...	... ± ...	... ± ...
IQ Tau	24.67 ± 0.84	13.81 ± 0.47	... ± ...	... ± ...	... ± ...	2.37 ± 0.16	2.13 ± 0.04	0.66 ± 0.02	... ± ...
UY Aur	46.27 ± 0.97	16.32 ± 0.34	3.36 ± 0.07	2.74 ± 0.05	2.74 ± 0.00	1.43 ± 0.06	1.42 ± 0.04	... ± ...	... ± ...
GI Tau	25.33 ± 1.60	14.41 ± 0.91	1.34 ± 0.00	1.04 ± 0.07	1.51 ± 0.00	2.89 ± 0.06	3.07 ± 0.03	1.51 ± 0.02	0.91 ± 0.00
HP Tau	12.44 ± 0.59	2.13 ± 0.10	... ± ...	... ± ...	... ± ...	... ± ...	... ± ...	... ± ...	... ± ...

Note. Note that we use positive EW to indicate emission. The units are Å.

from a residual curve generated by subtracting the flare-free light curve from the original curve. This method allows us to accurately quantify the properties of each flare, including its amplitude, duration, and energy release. We further examine the candidates for their authenticity by visually inspecting the TPF to generate the light curve of each pixel, using the Python package Lightkurve (Lightkurve Collaboration et al. 1812) and the method described by Wu et al. (2015). In our sample, we detect flares in the light curves of three stars: BP Tau (three flares), DN Tau (six flares), and FN Tau (four flares), for a total of 13 flares, and some of them are multiflare events. The light-curve profiles of these flares are shown in Figure 15. However, the absence of flares in other stars does not necessarily mean that they are not flaring stars. For example, Tofflemire et al. (2017) and Kóspál et al. (2018) both detected several flare events in DQ Tau from optical and Kepler observations, whereas we did not detect any flares in DQ Tau from the TESS observation in this study. It is possible that there are

Table 6
Mass Accretion Rates of 16 CTTSs Derived from LAMOST Spectra in This Study

Name (1)	$\dot{M}_{H\alpha}$ (2)	$\dot{M}_{H\beta}$ (3)	$\dot{M}_{Ca\,II8498}$ (4)	$\dot{M}_{Ca\,II8542}$ (5)	$\dot{M}_{Ca\,II8662}$ (6)	$\dot{M}_{HeI4771}$ (7)	$\dot{M}_{He\,I5875}$ (8)	$\dot{M}_{He\,I6678}$ (9)	$\dot{M}_{HeI7065}$ (10)
AA Tau	0.835 ± 0.010	1.399 ± 0.016	... ± ...	... ± ...	... ± ...	1.713 ± 0.028	1.625 ± 0.026	0.845 ± 0.021	... ± ...
BP Tau	5.591 ± 0.002	5.831 ± 0.002	... ± ...	... ± ...	... ± ...	8.488 ± 0.092	... ± ...	... ± ...	... ± ...
CI Tau	1.133 ± 0.035	0.889 ± 0.027	6.902 ± 0.033	4.994 ± 0.016	4.567 ± 0.004	0.745 ± 0.009	2.154 ± 0.037	2.588 ± 0.095	... ± ...
DL Tau	1.314 ± 0.008	2.090 ± 0.013	9.859 ± 0.353	5.212 ± 0.000	6.757 ± 0.061	2.714 ± 0.050	3.541 ± 0.015	4.527 ± 0.080	5.378 ± 0.055
DN Tau	0.993 ± 0.029	2.745 ± 0.081	... ± ...	... ± ...	... ± ...	... ± ...	2.252 ± 0.090	... ± ...	... ± ...
DQ Tau	1.022 ± 0.011	0.831 ± 0.009	... ± ...	... ± ...	... ± ...	0.860 ± 0.043	0.706 ± 0.030	... ± ...	... ± ...
FN Tau	0.091 ± 0.001	0.087 ± 0.001	... ± ...	... ± ...	... ± ...	0.099 ± 0.000	0.107 ± 0.001	... ± ...	... ± ...
GG Tau	6.349 ± 0.095	9.110 ± 0.136	3.579 ± 0.052	2.901 ± 0.017	2.961 ± 0.051	... ± ...	5.937 ± 0.003	... ± ...	... ± ...
GO Tau	0.209 ± 0.007	0.323 ± 0.012	... ± ...	... ± ...	... ± ...	0.592 ± 0.008	0.289 ± 0.014	... ± ...	... ± ...
Haro 6-13	0.402 ± 0.006	... ± ...	2.424 ± 0.000	1.353 ± 0.000	2.083 ± 0.000	... ± ...	... ± ...	... ± ...	... ± ...
HK Tau	1.983 ± 0.022	2.517 ± 0.028	... ± ...	... ± ...	... ± ...	... ± ...	1.994 ± 0.033	... ± ...	... ± ...
HL Tau	0.285 ± 0.034	0.185 ± 0.022	3.538 ± 0.045	12.163 ± 0.000	2.959 ± 0.019	... ± ...	... ± ...	... ± ...	... ± ...
IQ Tau	4.450 ± 0.100	7.774 ± 0.175	... ± ...	... ± ...	... ± ...	13.949 ± 0.573	15.126 ± 0.174	18.257 ± 0.421	... ± ...
UY Aur	4.017 ± 0.055	9.112 ± 0.126	3.915 ± 0.051	2.616 ± 0.025	2.842 ± 0.000	9.620 ± 0.263	5.433 ± 0.099	... ± ...	... ± ...
GI Tau	0.296 ± 0.012	1.072 ± 0.045	0.369 ± 0.000	0.249 ± 0.009	0.425 ± 0.000	3.295 ± 0.043	1.735 ± 0.012	2.604 ± 0.022	2.021 ± 0.004
HP Tau	0.079 ± 0.002	0.024 ± 0.001	... ± ...	... ± ...	... ± ...	... ± ...	... ± ...	... ± ...	... ± ...

Note. The units of all measurements shown here are $\times 10^{-9}\ M_{\odot}\ yr^{-1}$.
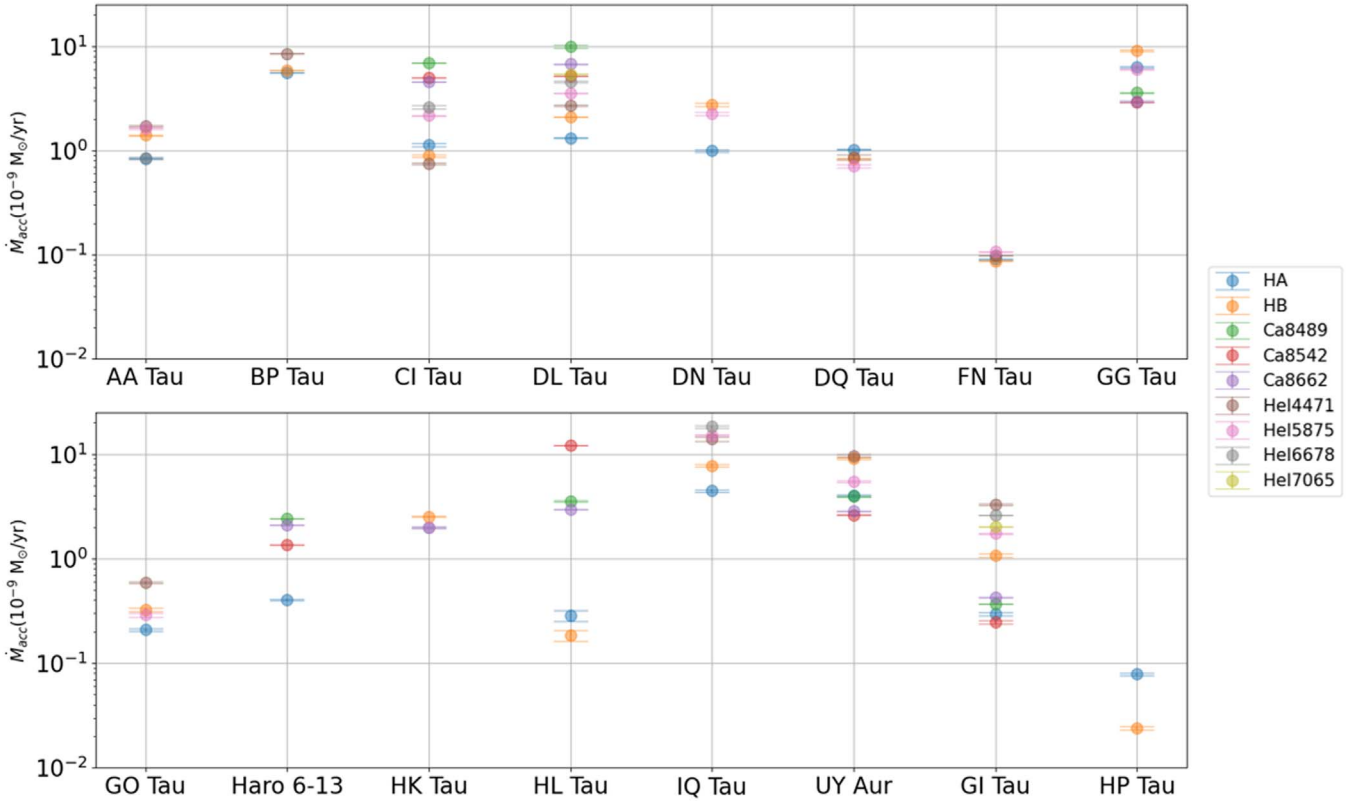
Figure 14. The distribution of mass accretion rates derived from all available emissions in the spectra of our CTTSs. The names of the stars marked with an asterisk in the upper right indicate that they are binary or multistar systems.

microflares with amplitudes or durations that are too small to be detected by TESS.

4.3.2. Flare Amplitude and Energy

The amplitude of the flare profile as a function of time can be determined using Equation (8). The flare energy is estimated using an equivalent duration (ED) method defined as follows (Gershberg 1972):

$$\text{ED} = \int \frac{\Delta F(t)}{\widetilde{F}} dt. \tag{12}$$

It represents the time it takes for a nonflaring star to emit the same amount of energy as that released during a given flare. Therefore, this quantity can be used to estimate the energy of the flare by multiplying it by the quiescent stellar flux in the telescope bandpass,

$$E_{f,\lambda} = \text{ED} \times F_{*,\lambda}, \tag{13}$$

and the corresponding quiescent stellar flux of the star can be estimated from

$$F_{*,\lambda} = 4\pi R_*^2 \sigma T_*^4 f_\lambda(T_*). \tag{14}$$

Here R_* is the stellar radius, T_* is the effective temperature, and σ is the Stefan–Boltzmann constant. Parameter f_λ is the same function as appeared first in Equation (9), which is a bandpass response factor as a function of temperature for the wavelength (λ) band, and in this case $\lambda = \text{TESS}$, i.e., the fractional response function of TESS (see Figure 12).

The amplitudes, duration, timing at peak in BTJD, and released energy of detected flares are listed in Table 7. These flares have

energy levels ranging from 2×10^{34} erg to 6×10^{35} erg. The flare with the highest amplitude of 0.22 is observed in BP Tau, with a duration of about 76 minutes and energy of 1×10^{35} erg. The most energetic flare in our sample is observed in FN Tau, with an energy of 6.3×10^{35} erg, an amplitude of 0.09, and a duration of 438 minutes. Furthermore, given the duration of the flares, these events likely originate from the localized magnetic reconnections near the stellar surface.

4.3.3. Flare Frequency Distribution

The flare activity of a star can be characterized by its flare frequency distribution, which can be described by a linear relationship expressed in logarithmic form as

$$\log N = a + \beta \log E, \tag{15}$$

where N is the cumulative frequency of flares with released energy E. The slope of the distribution, represented by the coefficient β, can provide information about the properties of the star's flare activity. If $\beta < -1$, then most of the total energy emitted by the flares comes from small flares, while for $\beta > -1$ stronger flares dominate the energy output. The flare frequency distribution power law can also be expressed in differential form as

$$dN \propto E^{-\alpha} dE, \tag{16}$$

where dN is the number of flares with energies in the range of E and $E + dE$, and $\alpha = 1 - \beta$ (Hawley et al. 2014). We use the maximum likelihood estimator (MLE) for α as derived by

BP Tau's flares:
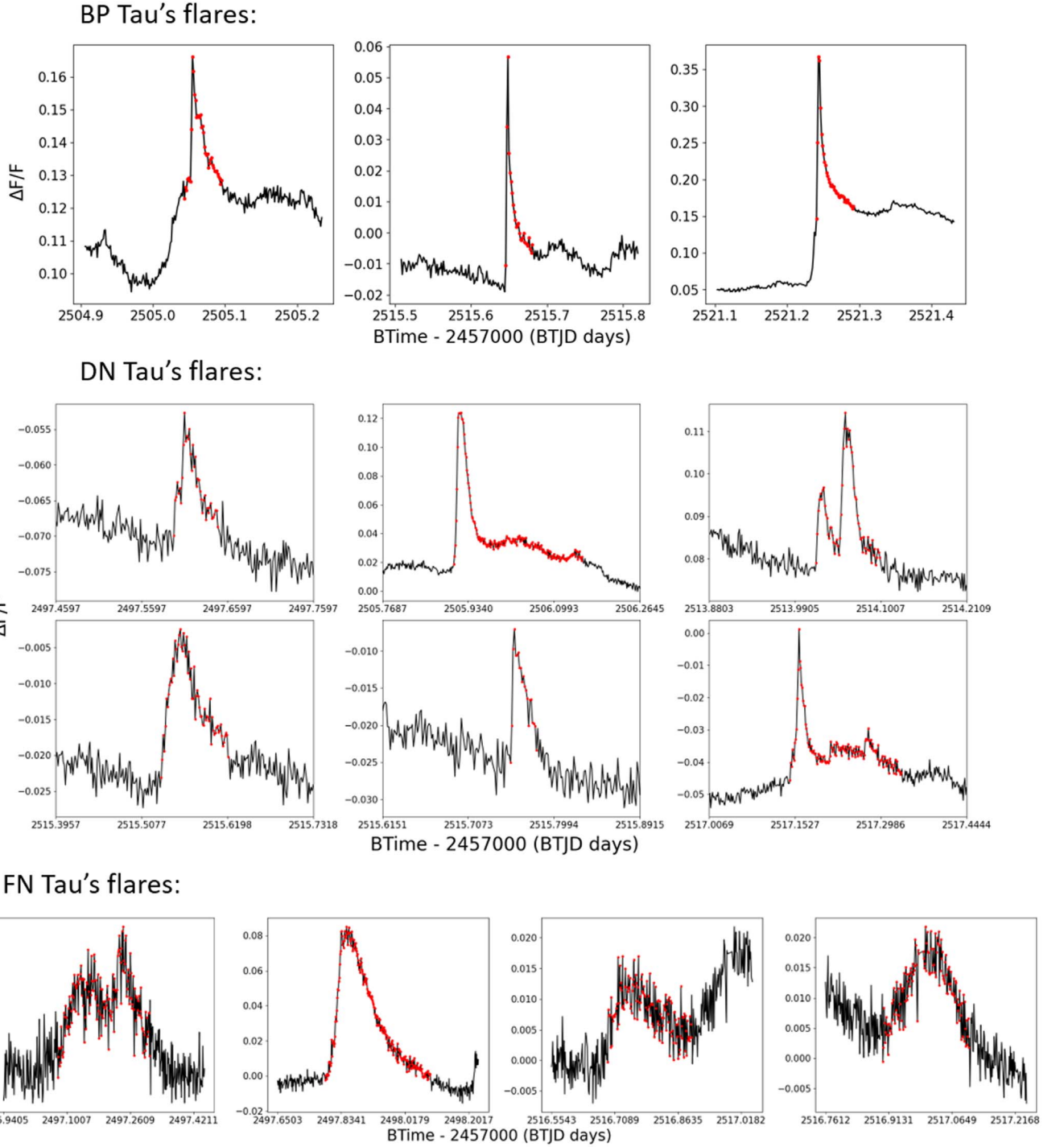

DN Tau's flares:

FN Tau's flares:

Figure 15. The profiles of 13 flare events detected in the Section 43 and 44 TESS light curves of BP Tau (three flares), DN Tau (six flares), and FN Tau (four flares).

Clauset et al. (2009),

$$\alpha = 1 + n \left[\sum_{i=1}^{n} \ln \frac{E_i}{E_{\min}} \right]^{-1}, \quad (17)$$

and the error for α can be estimated from

$$\sigma_\alpha = \frac{\sqrt{n+1}(\alpha - 1)}{n}. \quad (18)$$

Here n is the number of flare samples, and $E_{\min}$ is the minimum value of the energy of the observed flares. By setting

$E_{\min} = 2.2 \times 10^{34}$ erg and $n = 13$, we have calculated the value of α to be 1.68 ± 0.20. From this, we can derive the linear slope of the logarithmic flare frequency distribution, which is represented by $\beta = -0.68 \pm 0.20$ and a constant a of 24.32. Figure 16 shows the flare frequency distribution and its best-fit power-law slope for our CTTS sample. These results suggest that strong flares with high energy dominate the flare activity of these stars. The power-law distribution also indicates that our sample stars exhibit extreme flare activity, with the ability to generate flares with energy levels stronger than $E = 1 \times 10^{34}$ erg about 12 times per year. This is in stark
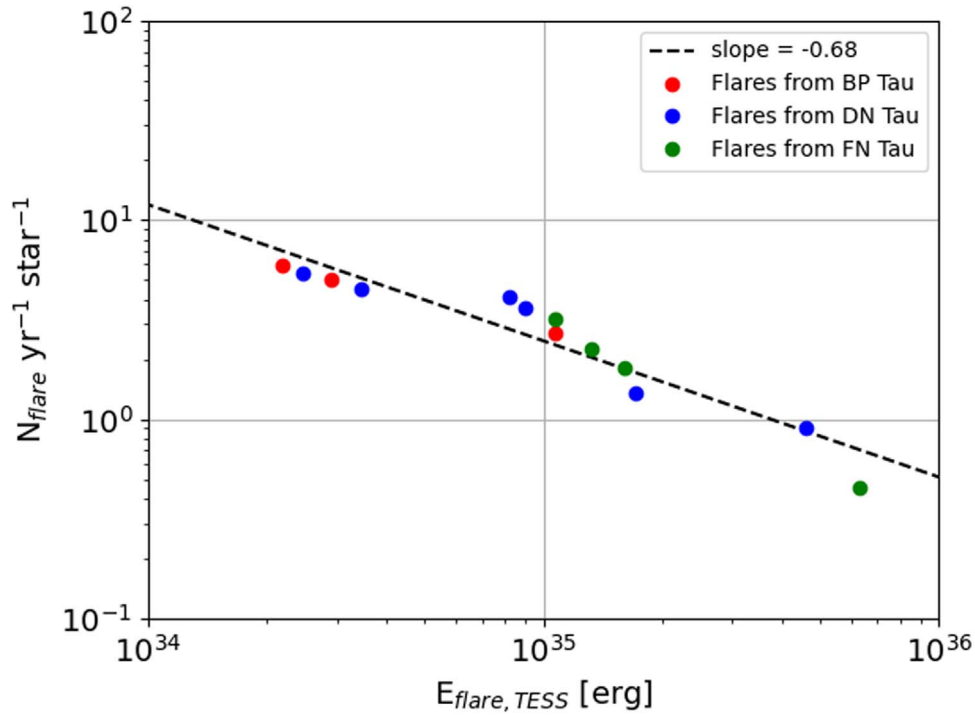
Figure 16. The flare frequency distribution and the best-fit power-law function with a slope of -0.68 ± 0.20 of our CTTS sample based on 13 detected flares in this study.

Table 7
13 Flares Detected in the TESS Light Curves of BP Tau, DN Tau, and FN Tau

Source	Amplitude	$E_{f,\text{tess}}$ log(erg)	t_{start} (BT−2,457,000)	t_{peak} (BT−2,457,000)	t_{end} (BT−2,457,000)	Duration (days)
	(1)	(2)	(3)	(4)	(5)	(6)
BP Tau	0.042	34.46	2505.0438	2505.0549	2505.0980	0.053
BP Tau	0.067	34.34	2515.6458	2515.6486	2515.6833	0.036
BP Tau	0.221	35.03	2521.2405	2521.2433	2521.2947	0.053
DN Tau	0.017	34.54	2497.5972	2497.6097	2497.6514	0.053
DN Tau	0.104	35.66	2505.9062	2505.9201	2506.1562	0.249
DN Tau	0.035	34.95	2514.0178	2514.0553	2514.1025	0.083
DN Tau	0.019	34.91	2515.5332	2515.5582	2515.6235	0.089
DN Tau	0.017	34.39	2515.7526	2515.7568	2515.7832	0.029
DN Tau	0.046	35.23	2517.1444	2517.1597	2517.3361	0.190
FN Tau	0.020	35.12	2497.0780	2497.2433	2497.3128	0.233
FN Tau	0.087	35.80	2497.7878	2497.8489	2498.0934	0.304
FN Tau	0.017	35.03	2516.6918	2516.7668	2516.8987	0.206
FN Tau	0.023	35.21	2516.8987	2517.0015	2517.1085	0.208

Note. Column (1): flare peak amplitude. Column (2): flare energy in the TESS band. Column (3): start time of the flare. Column (4): time of flare peak. Column (5): end time of the flare. Column (6): duration of the flare in units of days.

contrast to solar-type stars, which produce flares of this magnitude only once every 35–40 yr (Shibayama et al. 2013). Even one of the most flare-active young M stars, Wolf 359, can produce only one such flare a year (Lin et al. 2021).

4.4. The Changes of the Variability Classes

The changes in the variability behavior of the CTTSs can be attributed to the inner disk structure responsible for the stellar occultation, which can undergo significant changes in just a few years, transitioning from a stable and well-organized geometry with a consistent inner disk warp to a more disordered distribution of dust (e.g., McGinnis et al. 2015). Another explanation is the stability of the accretion regime. Initially, the accretion geometry may consist of a main accretion funnel in each hemisphere, with the base of each funnel corresponding to the stable inner disk warp. However, over time, this geometry may become unstable, resulting in the formation of random accretion funnels (e.g., Kurosawa & Romanova 2013). Cold spots due to the strong magnetic field of CTTSs might be able to cover a large fraction of stellar surface, which is similar to magnetically active low-mass stars (e.g., Yang et al. 2017; Lin et al. 2021), and the changes of their distribution and sizes may be also
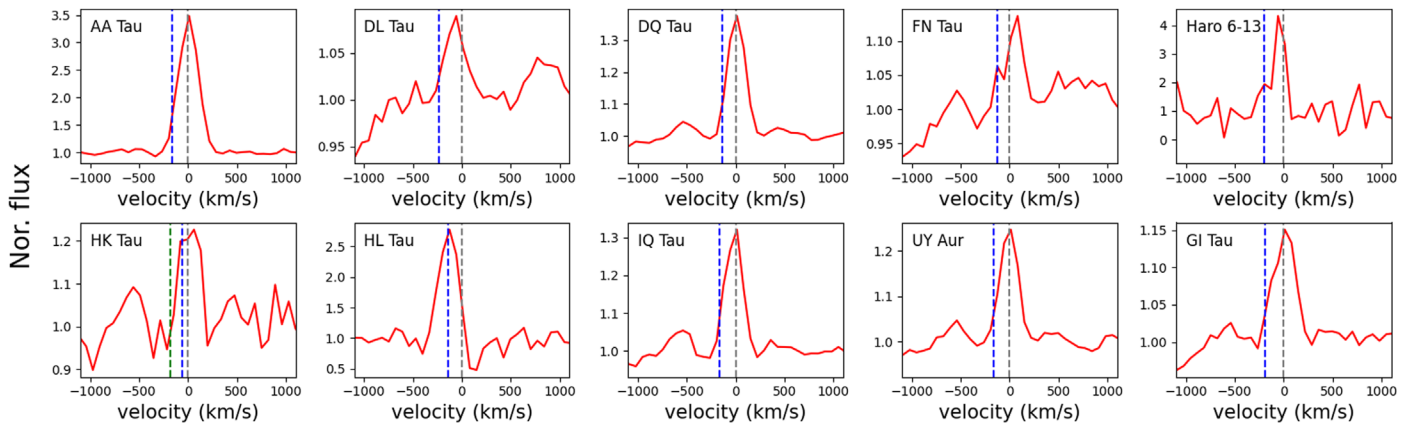
Figure 17. The velocity profiles of [O I] λ6300 lines of 10 CTTSs in our sample. In each panel, the gray vertical dashed line indicates the center of the line, and the blue dashed line marks the wind velocity of the blueshifted wind or peak of the line. In a special case of HK Tau, we also show a green dashed line to represent the blueshifted wind velocity, which is likely originating from a companion of the binary system, HK Tau A, and the blueshifted peak velocity marked with a blue dashed line belongs to the other companion of the system, HK Tau B.

reflected in the changes of variability behaviors (e.g., Frasca et al. 2005).

Ten stars in our sample were previously observed by K2 Campaign 13 (AA Tau, DQ Tau, GO Tau, Haro 6-13, HK Tau, HL Tau, and IQ Tau) or TESS Section 19 (BP Tau, FN Tau, and UY Aur), and their light curves were analyzed and classified for variability by Cody et al. (2022) and Robinson et al. (2022). The variability classes given by Cody et al. (2022) and Robinson et al. (2022) are also listed in Table 4. By comparing the variability classes given by Cody et al. (2022) based on the K2 C13 data observed about 4 yr ago, we find that most of the stars (six out of seven) change their variability classes, with the exception of DQ Tau. Specifically, AA Tau changes from "S" to "QPS," GO Tau changes from "U" to "APD," Haro 6-13 changes from "S" to "B," HK Tau changes from "QPS" to "QPD," IQ Tau changes from "QPS" to "P," and HL Tau changes from "QPS" to "QPD." In contrast, the variability classes of BP Tau and FN Tau do not change compared to those derived by Robinson et al. (2022) using TESS Section 19 light curves from about 600 days ago. Even though UY Aur changes from "B" to "QPS" in 600 days, we still see a burst-like event at BJTD = 2491 in its TESS Section 43 light curve. These findings may suggest that the long-term timescale of the variation associated with, for example, the stable/unstable accretion regime and inner disk warp due to the star–disk interaction of the CTTSs is in the range of about 1.6–4 yr or longer. However, it remains to be determined whether these changes occur in a cyclical or random manner. For instance, Haro 6-13 changing from the "B" type back to the "S" type, or to any other type, would require further investigation through continuous monitoring in the future.

4.5. Effect of the Inclination on the Spectra, Accretion, and Variability Properties

The spectral properties of the CTTSs have been predicted to be correlated with the inclination of the system, especially with the broad or high-velocity component of the forbidden line profile (e.g., Hartigan et al. 1995). The high-velocity components are generally believed to originate in fast outflows that keep thrusting material into interstellar space in the form of jets. Among the known forbidden lines, the ones with the most distinctive high-velocity component spectral features are the [N II] lines at 6548 and 6583 Å, which behave as blueshifted

emission with a well-defined peak (Hirth et al. 1997). Nevertheless, the resolving power of the LAMOST observations is not high enough to distinguish the [N II] lines from Hα emission; thus, we cannot derive the outflow velocity from these lines using the data we have in this study.

Additional forbidden lines that can provide insight into the wind velocity observed by LAMOST are the [O I] line at 6300 Å, [S II] lines at 6716 and 6731 Å, and [Ca II] lines at 7291 and 7323 Å. While the blueshifted emission of the [O I] line may not display a distinct peak when compared to the [N II], [S II], and [Ca II] lines, the extended blue wing can be interpreted as an indicator of the projected wind velocity (Appenzeller & Bertout 2013). Out of the sample CTTSs, 10 stars exhibit [O I] lines in their LAMOST spectra, while [S II] lines have only been detected in AA Tau and HL Tau. Moreover, [Ca II] lines are observed in only one star, HL Tau.

We estimate the projected wind velocity by using the blue edge of the line profile, with flux reaching 25% of the peak value when the line shows no clear blue peak. Because of the low resolution of the LAMOST data, for those profiles showing a blue peak, the velocity is directly estimated from the wavelength of the peak. The LAMOST [O I] line, [S II] line, and [Ca II] line velocity profiles of the CTTSs are shown in Figures 17, 18, and 19, respectively. The results of [O I], [S II], and [Ca II] velocity measurements are listed in Table 8. For stars where velocity measurements are available from not only [O I] but also [S II] and [Ca II], i.e., AA Tau and HL Tau, the results are consistent across all lines. We note that there are two [O I] velocity results for a binary HK Tau. The diameter of LAMOST's fiber is about 3″3, and the angular separation between HK Tau A and HK Tau B is about 2″3. Thus, LAMOST observation cannot resolve these two stars separately. We detect a blueshifted peak of the [O I] line at a wind velocity of $-56.49\,\mathrm{km\,s^{-1}}$, which may have originated from the edge-on system HK Tau B with an inclination of 84°. The velocity derived from the blue edge of the line with a value of $-182.88\,\mathrm{km\,s^{-1}}$ belongs to HK Tau A, which has a relatively face-on disk with an inclination of $i = 56°9$. The comparison between the inclinations and [O I] line-derived projected wind velocity is shown in Figure 20. Our results show a positive correlation between the cosine of inclination and the projected wind velocity, consistent with the trend observed by Appenzeller & Bertout (2013).
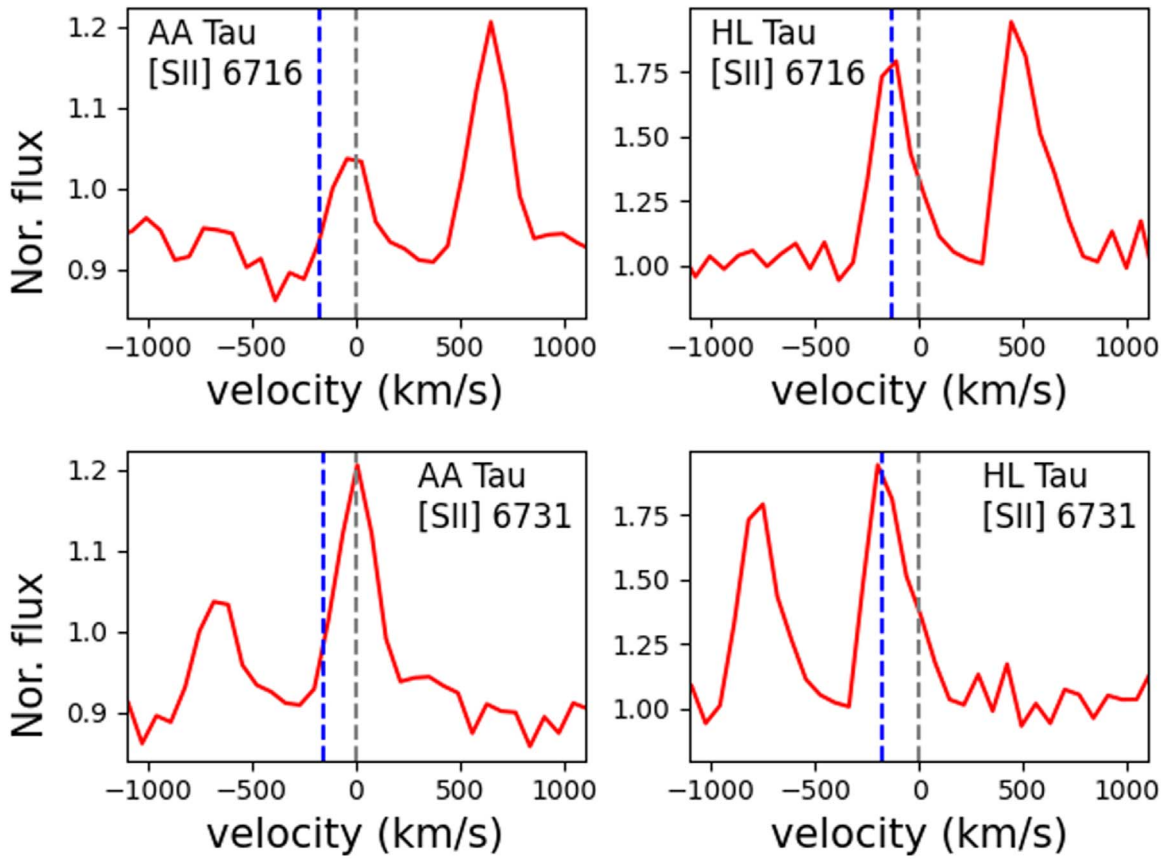
Figure 18. The velocity profiles of [S II] lines observed in the spectra of AA Tau and HL Tau. In each panel, the gray vertical dashed line indicates the center of the line, and the blue dashed line marks the wind velocity of the blueshifted wind or peak of the line.
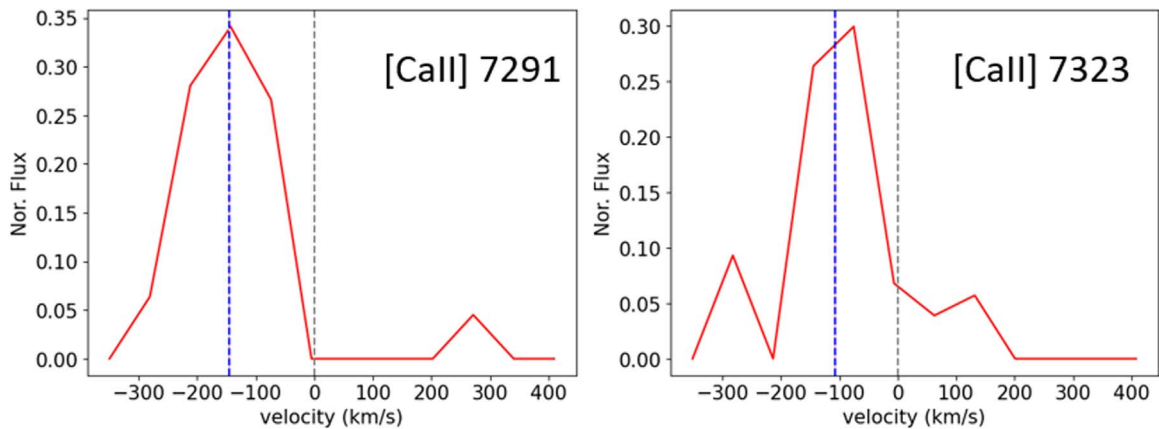

Figure 19. The velocity profiles of [Ca II] lines of HL Tau. The gray vertical dashed line indicates the center of the line, and the blue dashed line marks the wind velocity of the blueshifted peak of the line.

The inclination angle of a CTTS may have an impact on the estimation of its mass accretion rate to some degree. This is because the varying geometric angle of the disk could obscure areas emitting accretion-associated emission from the line of sight, leading to uncertainties in the measurement. However, our analysis indicates that there is no significant correlation between the inclination angle and the log spectra–derived mass accretion rates (see Figure 21) with a Pearson's correlation coefficient of 0.34 for Hα's measurement, and the correlation coefficients are even lower for the results from other emissions. One possibility is that the emission regions driven by accretion are uniformly distributed on the surface of

the CTTS, making the effect of disk obscuration negligible. Another possible explanation is that the properties of the inner disk may play a more significant role than those of the outer disk. Several studies have reported misalignments between the inner and outer disks. For example, the inner disk of AA Tau has an inclination angle of $i = 75°$, closer to edge-on (Bouvier et al. 2003; O'Sullivan et al. 2005), while the outer disk has an inclination angle of $i = 59°$ (Loomis et al. 2017). Unfortunately, information on the inclination angle of the inner disk for our sample stars, except for AA Tau, is not available. Further studies using high-resolution double-peaked Keplerian line spectroscopic observations or spatially resolved
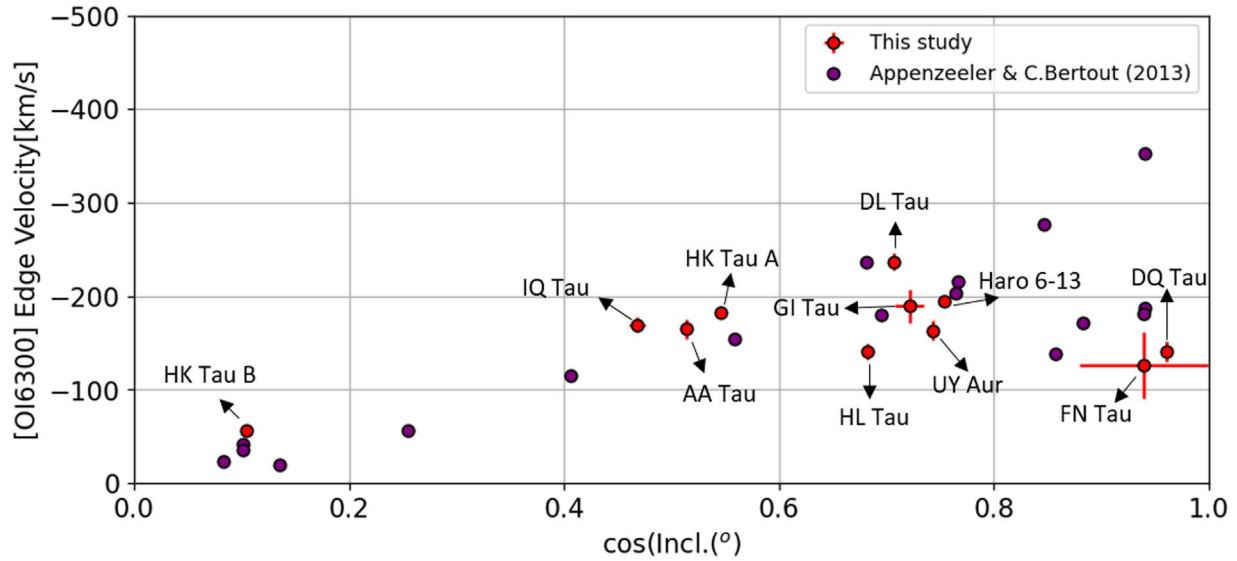
Figure 20. The comparison between CTTSs' [O I] λ6300 projected wind velocities (vertical axis) and inclinations in terms of cosine angle (horizontal axis). The purple circles represent the data from Appenzeller & Bertout (2013), and the red circles are the data in this study.

Table 8
The Projected Wind Velocities of CTTSs Observed by LAMOST

Name	[O I] λ6300 v_{wind} (km s^{-1})	[S II] λ6716 v_{wind} (km s^{-1})	[S II] λ6731 v_{wind} (km s^{-1})	[Ca II] λ7291 v_{wind} (km s^{-1})	[Ca II] λ7323 v_{wind} (km s^{-1})
AA Tau	-164.79 ± 10.22	-170.44 ± 8.40	-152.39 ± 10.20	$\cdots \pm \cdots$	$\cdots \pm \cdots$
DL Tau	-236.64 ± 9.57	$\cdots \pm \cdots$	$\cdots \pm \cdots$	$\cdots \pm \cdots$	$\cdots \pm \cdots$
DQ Tau	-140.74 ± 11.44	$\cdots \pm \cdots$	$\cdots \pm \cdots$	$\cdots \pm \cdots$	$\cdots \pm \cdots$
FN Tau	-125.50 ± 35.53	$\cdots \pm \cdots$	$\cdots \pm \cdots$	$\cdots \pm \cdots$	$\cdots \pm \cdots$
Haro 6-13	-194.49 ± 6.31	$\cdots \pm \cdots$	$\cdots \pm \cdots$	$\cdots \pm \cdots$	$\cdots \pm \cdots$
HK Tau A	$-182.88 \pm ...$	$\cdots \pm \cdots$	$\cdots \pm \cdots$	$\cdots \pm \cdots$	$\cdots \pm \cdots$
HK Tau B	-56.49 ± 4.55	$\cdots \pm \cdots$	$\cdots \pm \cdots$	$\cdots \pm \cdots$	$\cdots \pm \cdots$
HL Tau	-140.74 ± 9.11	-132.43 ± 31.01	-152.25 ± 34.56	-146.17 ± 24.44	-107.96 ± 9.82
IQ Tau	-169.29 ± 7.54	$\cdots \pm \cdots$	$\cdots \pm \cdots$	$\cdots \pm \cdots$	$\cdots \pm \cdots$
UY Aur	-163.31 ± 10.92	$\cdots \pm \cdots$	$\cdots \pm \cdots$	$\cdots \pm \cdots$	$\cdots \pm \cdots$
GI Tau	-189.32 ± 17.51	$\cdots \pm \cdots$	$\cdots \pm \cdots$	$\cdots \pm \cdots$	$\cdots \pm \cdots$

observations using infrared interferometry on The Very Large Telescope Interferometer (VLTI) may be required to address this issue.

The type of photometric variability of CTTSs is dominated by the accretion and dark spots located on the photosphere and the surrounding disk; thus, it could be geometric viewing angle dependent. Cody & Hillenbrand (2018) found a positive correlation between the M value they estimated and the inclination Barenfeld et al. (2017) gave, so that dippers and QPS sources tend to have high inclinations, while bursters and stochastic sources have low inclinations. However, due to the substantial uncertainties associated with the inclination measurements, they cautiously stated this observed tendency. A more recent study by Robinson et al. (2022), based on CTTSs with lower inclination uncertainties, found little evidence for a strong correlation between disk inclination and M value (see Figure 2 in their paper). The top panel of Figure 22 illustrates the relationship between inclination and M value of CTTSs, including our samples and those from Robinson et al. (2022). Our analysis reveals a relatively strong and positive correlation between M value and inclination, with a Pearson's value of 0.61 ± 0.03, compared to the results given by Cody & Hillenbrand (2018) and Robinson et al. (2022).

On the other hand, we find an indistinct and negative correlation between the periodicity metric Q value and inclination with a Pearson's value of -0.54 ± 0.03 (see the bottom panel of Figure 22) for our targets. This is consistent with the conclusion given by Robinson et al. (2022), who also found the weak inverse correlation between disk inclination and periodicity metric of Taurus CTTSs. Furthermore, the distribution of variability classes in the inclination–Q space in our study is similar to that of Taurus members studied by Cody et al. (2022), as shown in Figure 7 of their paper. Nevertheless, it is possible that such distribution and the correlation between M value and inclination, as well as the correlation between periodicity metric Q value and inclination, could vary over time owing to the changing variability classes of CTTSs.

5. Summary

We present a comprehensive study of 16 low-mass CTTSs in TMC for their mass accretion and luminosity variability properties by using LAMOST low-resolution spectra and TESS photometric light curves.

From the LAMOST spectra, the mass accretion rates of 16 CTTSs have been estimated using Hα, Hβ, Ca II, and He I emissions as indicators. The average mass accretion rate of all our
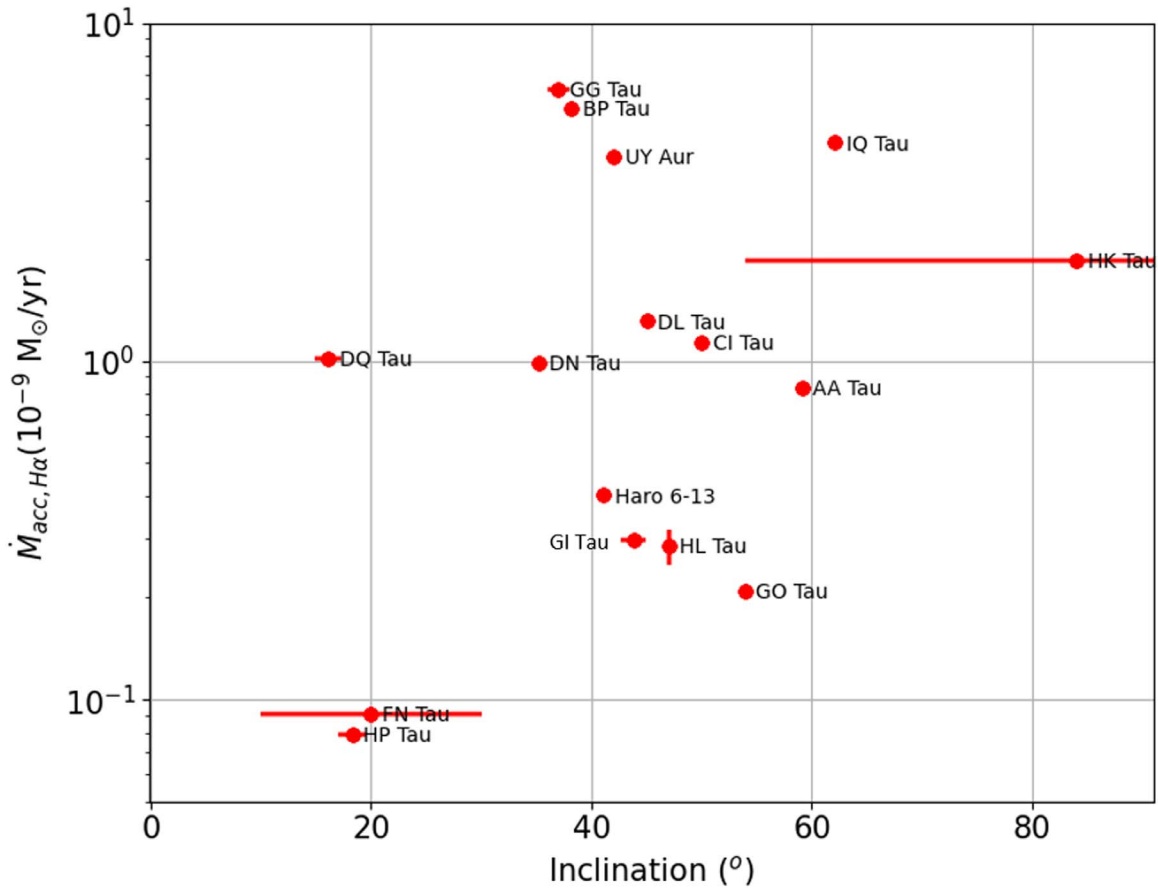
Figure 21. The relationship between the inclination and mass accretion rates derived from the Hα emission luminosities. The Pearson's correlation coefficient is about 0.34, indicating that the correlation is not significant.

samples based on Hα lines is found to be $1.76 \times 10^{-9}\ M_\odot\ \mathrm{yr}^{-1}$. Not all targets in the sample have measurable EWs for the other emission lines, which means that not all corresponding mass accretion rates could be estimated. HL Tau has the largest dispersion of the spectral-derived mass accretion rates with a CV value of 1.15, which is the ratio of the standard deviation to the mean. The reason for this huge dispersion remains unclear. On the other hand, the lowest-dispersion CV value is found in FN Tau, which is 0.08.

We also compute the time-series mass accretion rates based on the TESS light curve, ZTF, and ASAS-SN survey for the stars DL Tau and Haro 6-13, which are identified to be the bursters according to their brightness variability asymmetry metric M values of -0.63 and -0.31, respectively (Cody et al. 2014). In total over about 50 days, the average accretion rates of DL Tau and Haro 6-13 are $2.5 \times 10^{-9}\ M_\odot\ \mathrm{yr}^{-1}$ and $1.4 \times 10^{-11}\ M_\odot\ \mathrm{yr}^{-1}$, respectively. The rate of DL Tau is consistent with the mean value of the mass accretion derived from LAMOST. However, for Haro 6-13, this rate is generally lower compared to the LAMOST estimate. We further investigate whether the mass accretion mechanisms of these two stars are dominated by steady or burst accretion. By assuming the average rates obtained from LAMOST emission measurement as the steady rates, the mass accretions in DL Tau and Haro 6-13 are dominated by the steady process.

We have detected 13 flares in total in BP Tau, DN Tau, and FN Tau. The amplitude, duration, timing at peak in BTJD, and released energy of detected flares are determined, with the most

energetic flare observed in FN Tau with an energy of 6.3×10^{35} erg. The power-law flare frequency distribution with a slope of $\beta = -0.68 \pm 0.20$ indicates that the flare activity of the CTTSs is dominated by a strong flare with high energy. Our analysis of the flare frequency distribution also reveals that the stars in our sample display extremely high levels of flare activity with the capability of producing flares with energy greater than $E = 1 \times 10^{34}$ erg up to 12 times per year, which is a significant deviation from solar-type stars and young M dwarfs.

Ten stars in our sample were previously observed and classified for variability by Cody et al. (2022) and Robinson et al. (2022). Comparing the variability classes from Cody et al. (2022) based on K2 Campaign 13 data from about 4 yr ago, we found that most of the stars (six out of seven) showed changes in their variability, except for DQ Tau. In comparison with the results from Robinson et al. (2022), BP Tau and FN Tau's variability classes remained the same, while UY Aur changed from "B" to "QPS" in 600 days but still exhibited a burst-like event in its TESS Section 43 light curve. These findings suggest that the long-term timescale of variation in CTTSs could be between 1.6 and 4 yr or longer and require further investigation to determine whether changes occur cyclically or randomly.

The CTTSs' projected wind velocities in terms of the blue edge/peaks of [O I], [S II], and [Ca II] forbidden emissions detected in LAMOST are found to be correlated with the inclination, that is, stars with low inclination tend to have fast projected wind velocity. On the other hand, no tendency has
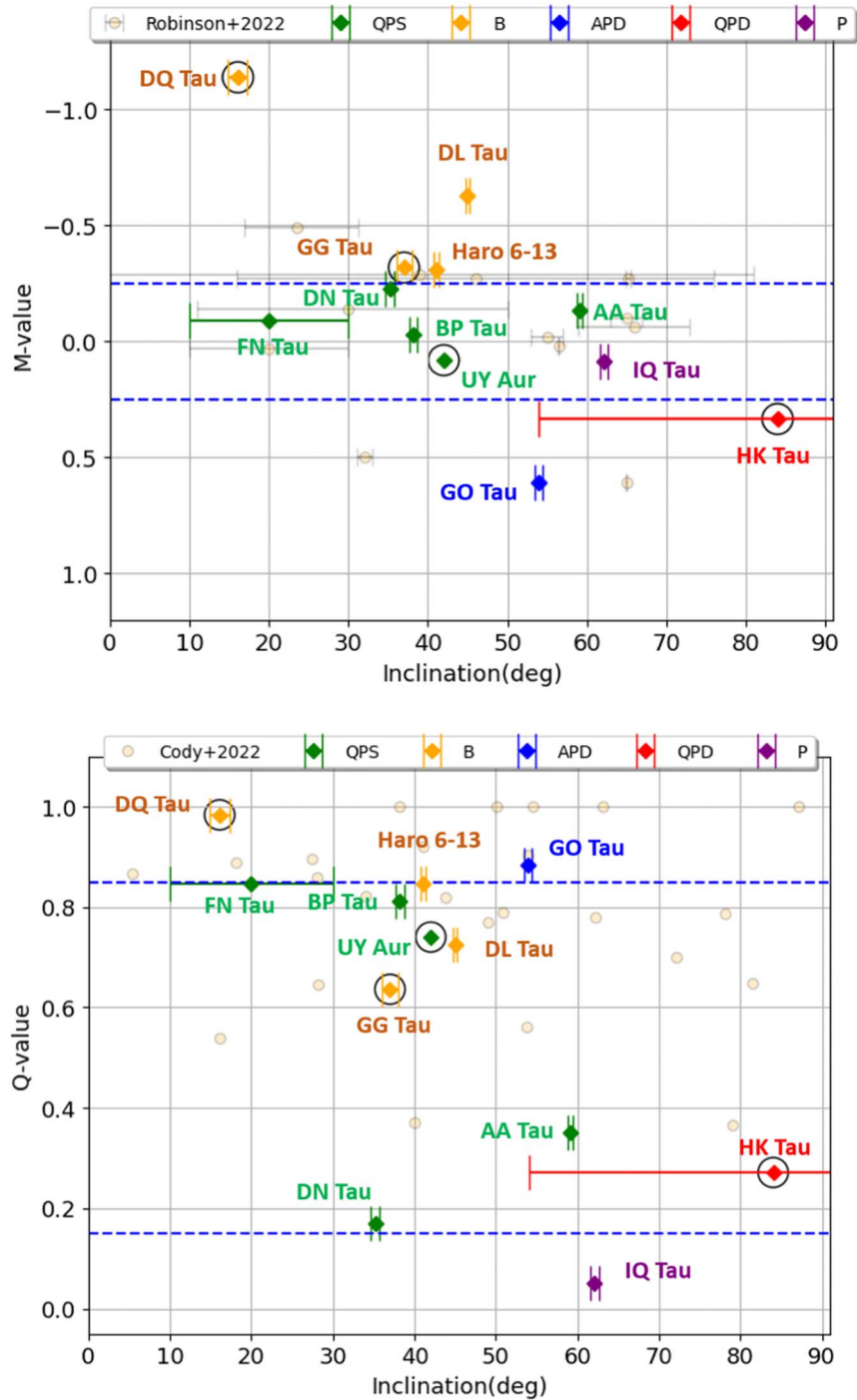
Figure 22. The relationship between the flux asymmetry metric M and the disk inclination of our CTTSs is shown in the top panel, and the relationship between the periodicity metric Q and the disk inclination is shown in the bottom panel. Our samples are represented by rhombus symbols, with different colors indicating different variability classes. We also include the results obtained by Robinson et al. (2022) for M vs. inclination and by Cody et al. (2022) for Q vs. inclination as the comparisons, shown as yellow circles. The stars surrounded by black open circles in this diagram are binary or multistar systems. Note that the large uncertainty of HK Tau's inclination is because it is an unresolved binary system in LAMOST observations, which is composed of two companions, HK Tau A with $i = 56°.9$ and HK Tau B with $i = 84°$. The blue dashed lines in both panels indicate the thresholds of bursting ($M < -0.25$), dipping ($M > 0.25$), periodic ($Q < 0.15$), and aperiodic ($Q > 0.85$).

been found between inclination and mass accretion rates derived from the spectral lines' luminosities. One possibility is that the regions of emission driven by accretion are distributed uniformly across the stellar surface, so the disk obscuration does not have much of an impact. Alternatively, it is possible that the properties of the inner disk are more important than those of the outer disk. There is evidence to suggest that the inner and outer disks of CTTSs can become misaligned owing to, e.g., magnetic warping. Unfortunately, in our sample, only AA Tau has a reported inner disk inclination angle. High-resolution double-peaked Keplerian line spectroscopic observations or spatially resolved observations using infrared interferometry on VLTI may be required for further studies of this topic.

The brightness variabilities of CTTSs have been also considered to be influenced by the inclinations to some degree. Our analysis reveals a relatively significant and positive correlation between M value and inclination, with a Pearson's value of 0.61 ± 0.03, compared to the results given by Cody & Hillenbrand (2018) and Robinson et al. (2022). We observed a weak negative correlation between the periodicity metric Q value and inclination for our targets, with a Pearson's value of -0.54 ± 0.03. This finding supports the conclusion reached by Robinson et al. (2022), who also reported a weak inverse correlation between disk inclination and the periodicity metric of Taurus CTTSs. Additionally, we found that the distribution of variability classes in the inclination–Q space is similar to that of Taurus members studied by Cody et al. (2022). However, since the variability classes of CTTSs can change over time, it is possible that the distribution and correlations between the M value and inclination, as well as between the periodicity metric Q value and inclination, could vary as well. Thus, further research is required to fully understand the long-term evolution of these correlations.

ORCID iDs

Chia-Lung Lin https://orcid.org/0000-0001-5989-7594
Wing-Huen Ip https://orcid.org/0000-0002-3140-5014
Yao Hsiao https://orcid.org/0000-0002-8915-8538
Yi-han Song https://orcid.org/0000-0001-7255-5003
A-Li Luo https://orcid.org/0000-0001-7865-2648

References

ALMA Partnership, Brogan, C. L., Pérez, L. M., et al. 2015, ApJL, 808, L3
Adams, F. C., Lada, C. J., & Shu, F. H. 1987, ApJ, 312, 788
Alcalá, J. M., Manara, C. F., Natta, A., et al. 2017, A&A, 600, A20
Alcalá, J. M., Natta, A., Manara, C. F., et al. 2014, A&A, 561, A2
Appenzeller, I., & Bertout, C. 2013, A&A, 558, A83
Argiroffi, C., Maggio, A., & Peres, G. 2007, A&A, 465, L5
Astropy Collaboration, Price-Whelan, A. M., Lim, P. L., et al. 2022, ApJ, 935, 167
Astropy Collaboration, Price-Whelan, A. M., Sipőcz, B. M., et al. 2018, AJ, 156, 123
Astropy Collaboration, Robitaille, T. P., Tollerud, E., et al. 2013, A&A, 558, A33
Audard, M., Briggs, K. R., Grosso, N., et al. 2007, A&A, 468, 379
Barenfeld, S. A., Carpenter, J. M., Sargent, A. I., et al. 2017, ApJ, 851, 85
Basri, G., & Bertout, C. 1989, ApJ, 341, 340
Bellm, E. C., Kulkarni, S. R., Graham, M. J., et al. 2019, PASP, 131, 018002
Bertout, C., Basri, G., & Bouvier, J. 1988, ApJ, 330, 350
Bouvier, J., Grankin, K. N., Alencar, S. H. P., et al. 2003, A&A, 409, 169
Camenzind, M. 1990, RvMA, 3, 234
Čemeljić, M., & Siwak, M. 2020, MNRAS, 491, 1057
Chambers, K. C., Magnier, E. A., Metcalfe, N., et al. 2016, arXiv:1612.05560
Clarke, C., Lodato, G., Melnikov, S. Y., et al. 2005, MNRAS, 361, 942
Clauset, A., Shalizi, C. R., & Newman, M. E. J. 2009, SIAMR, 51, 661
Close, L. M., Dutrey, A., Roddier, F., et al. 1998, ApJ, 499, 883
Cody, A. M., & Hillenbrand, L. A. 2018, AJ, 156, 71
Cody, A. M., Hillenbrand, L. A., & Rebull, L. M. 2022, AJ, 163, 212
Cody, A. M., Stauffer, J., Baglin, A., et al. 2014, AJ, 147, 82
Cody, A. M., Tayar, J., Hillenbrand, L. A., et al. 2013, AJ, 145, 79
Colombo, S., Orlando, S., Peres, G., et al. 2019, A&A, 624, A50
Costa, G., Orlando, S., Peres, G., et al. 2017, A&A, 597, A1
Czekala, I., Andrews, S. M., Torres, G., et al. 2016, ApJ, 818, 156
Ducati, J. R. 2002, yCat, 2237
Fang, M., van Boekel, R., Wang, W., et al. 2009, A&A, 504, 461
Feigelson, E. D., & Montmerle, T. 1999, ARA&A, 37, 363
Fischer, W. J., Hillenbrand, L. A., Herczeg, G. J., et al. 2022, arXiv:2203.11257
Flewelling, H. A., Magnier, E. A., Chambers, K. C., et al. 2020, ApJS, 251, 7
Frasca, A., Biazzo, K., Catalano, S., et al. 2005, A&A, 432, 647
Gaia Collaboration 2020, yCat, I/350
Gaia Collaboration, Brown, A. G. A., Vallenari, A., et al. 2021, A&A, 649, A1
Gershberg, R. E. 1972, Ap&SS, 19, 75
Getman, K. V., Broos, P. S., Kóspál, Á., et al. 2016, AJ, 152, 188
Giardino, G., Favata, F., Micela, G., et al. 2007, A&A, 463, 275
Guilloteau, S., Dutrey, A., & Simon, M. 1999, A&A, 348, 570

Gullbring, E., Hartmann, L., Briceño, C., et al. 1998, ApJ, 492, 323
Günther, H. M., Schmitt, J. H. M. M., Robrade, J., et al. 2007, A&A, 466, 1111
Harris, C. R, Millman, K. J., & van der Walt, S. J. 2020, Natur, 585, 357
Hartigan, P., Edwards, S., & Ghandour, L. 1995, ApJ, 452, 736
Hawley, S. L., Davenport, J. R., Kowalski, A. F., et al. 2014, ApJ, 797, 121
Herczeg, G. J., Cruz, K. L., & Hillenbrand, L. A. 2009, ApJ, 696, 1589
Herczeg, G. J., & Hillenbrand, L. A. 2008, ApJ, 681, 594
Herczeg, G. J., & Hillenbrand, L. A. 2014, ApJ, 786, 97
Hirth, G. A., Mundt, R., & Solf, J. 1997, A&AS, 126, 437
Hunter, J. D. 2007, CSE, 9, 90
IRSA 2022, Zwicky Transient Facility Image Service, IPAC, doi:10.26131/IRSA539
Jayasinghe, T., Kochanek, C. S., Stanek, K. Z., et al. 2018, MNRAS, 477, 3145
Jayasinghe, T., Stanek, K. Z., Kochanek, C. S., et al. 2019, MNRAS, 486, 1907
Jenkins, J. M., Twicken, J. D., McCauliff, S., et al. 2016, Proc. SPIE, 9913, 99133E
Kóspál, Á., Ábrahám, P., Zsidi, G., et al. 2018, ApJ, 862, 44
Kudo, T., Tamura, M., Kitamura, Y., et al. 2008, ApJL, 673, L67
Kurosawa, R., & Romanova, M. M. 2013, MNRAS, 431, 2673
Lightkurve Collaboration, Cardoso, J. V. de M., Hedges, C., et al. 1812, Lightkurve: Kepler and TESS time series analysis in Python, Astrophysics Source Code Library, ascl:1812.013
Lin, C.-L., Chen, W.-P., Ip, W.-H., et al. 2021, AJ, 162, 11
Lin, C.-L., Ip, W.-H., Hou, W.-C., et al. 2019, ApJ, 873, 97
Liu, Y., Henning, T., Carrasco-González, C., et al. 2017, A&A, 607, A74
Long, F., Herczeg, G. J., Harsono, D., et al. 2019, ApJ, 882, 49
Loomis, R. A., Öberg, K. I., Andrews, S. M., et al. 2017, ApJ, 840, 23
López-Santiago, J., Crespo-Chacón, I., Flaccomio, E., et al. 2016, A&A, 590, A7
Lynden-Bell, D., & Pringle, J. E. 1974, MNRAS, 168, 603
Maehara, H., Shibayama, T., Notsu, S., et al. 2012, Natur, 485, 478
Manara, C. F., Beccari, G., Da Rio, N., et al. 2013, A&A, 558, A114
Manara, C. F., Tazzari, M., Long, F., et al. 2019, A&A, 628, A95
Manara, C. F., Testi, L., Rigliaco, E., et al. 2013, A&A, 551, A107
Masci, F. J., Laher, R. R., Rusholme, B., et al. 2019, PASP, 131, 018003
Mathieu, R. D., Stassun, K., Basri, G., et al. 1997, AJ, 113, 1841
McGinnis, P. T., Alencar, S. H. P., Guimarães, M. M., et al. 2015, A&A, 577, A11
McKinney, W. 2010, in Proc. 9th Python Sci. Conf., ed. S. van der Walt & J. Millman (Austin, TX: SciPy), 51
Mendoza, V. E. E. 1968, ApJ, 151, 977
Muzerolle, J., Hillenbrand, L., Calvet, N., et al. 2003, ApJ, 592, 266
O'Sullivan, M., Truss, M., Walker, C., et al. 2005, MNRAS, 358, 632
Parker, E. N. 1963, ApJS, 8, 177
Percy, J. R., Grynko, S., Seneviratne, R., et al. 2010, PASP, 122, 753
Pinte, C., Dent, W. R. F., Ménard, F., et al. 2016, ApJ, 816, 25
Rebull, L. M., Stauffer, J. R., Cody, A. M., et al. 2020, AJ, 159, 273
Rigon, L., Scholz, A., Anderson, D., et al. 2017, MNRAS, 465, 3889
Robinson, C. E., Espaillat, C. C., & Rodriguez, J. E. 2022, ApJ, 935, 54
Rucinski, S. M., Matthews, J. M., Kuschnig, R., et al. 2008, MNRAS, 391, 1913
Salter, D. M., Kóspál, Á., Getman, K. V., et al. 2010, A&A, 521, A32
Sergison, D. J., Naylor, T., Littlefair, S. P., et al. 2020, MNRAS, 491, 5035
Shibayama, T., Maehara, H., Notsu, S., et al. 2013, ApJS, 209, 5
Simon, M., Guilloteau, S., Di Folco, E., et al. 2017, ApJ, 844, 158
Sousa, A. P., Alencar, S. H. P., Bouvier, J., et al. 2016, A&A, 586, A47
Tofflemire, B. M., Mathieu, R. D., Ardila, D. R., et al. 2017, ApJ, 835, 8
Venuti, L., Bouvier, J., Irwin, J., et al. 2015, A&A, 581, A66
Villenave, M., Ménard, F., Dent, W. R. F., et al. 2020, A&A, 642, A164
Virtanen, P., Gommers, R., Oliphant, T. E., et al. 2020, NatMe, 17, 261
Wu, C.-J., Ip, W.-H., & Huang, L.-C. 2015, ApJ, 798, 92
Yang, H., Liu, J., Gao, Q., et al. 2017, ApJ, 849, 36
Zhao, G., Zhao, Y.-H., Chu, Y.-Q., et al. 2012, RAA, 12, 723
Zucker, C., Speagle, J. S., Schlafly, E. F., et al. 2020, A&A, 633, A51